Aerodynamic Load Control in HAWT with Combined Aeroelastic Tailoring and Trailing-Edge Flaps

Bing Feng Ng, Rafael Palacios, Eric C. Kerrigan, J. Michael R. Graham and Henrik Hesse

1 Abstract

This paper presents an aeroservoelastic modeling approach to investigate dynamic load alleviation in large wind turbines with composite blades and trailing-edge aerodynamic surfaces. The tower and rotating blades are modeled using geometrically-nonlinear composite beams, and linearized about reference rotating conditions with potentially arbitrarily-large structural displacements. The aerodynamics of the rotor are represented using a linearized unsteady vortex-lattice method and the resulting aeroelastic system is written in a state-space description that is both convenient for model reductions and control design. A linear model of a single blade is then used to design an $\mathcal{H}_\infty$ regulator, capable of providing load reductions of up to 13% in closed-loop on the full wind turbine nonlinear aeroelastic model. When combined with passive load alleviation through aeroelastic tailoring, dynamic loads can be further reduced to 35%. While the separate use of active flap controls and passive mechanisms for load alleviation have been well-studied, an integrated approach involving the two mechanisms has yet to be fully explored and is the focus of this paper. Finally, the possibility of exploiting torsional stiffness for active load alleviation on turbine blades is also considered.

2 Introduction

Horizontal-Axis Wind Turbines (HAWT) have been steadily increasing in size since they were first considered for large-scale energy production, both in terms of tower height and rotor diameter [Barlas and van Kuik(2010)]. At the time of writing, the largest wind turbines in operation have rotors measuring above 120 m in diameter, but rotors of up to 160 m are already being developed. Larger blades are necessarily more flexible and, as a result, aeroelastic effects previously not seen in smaller rotors are beginning to surface [Hansen et al.(2006)Hansen, Sørensen, Voutsinas, Sørensen,
This has brought about new needs in terms of modeling requirements and poses new technological challenges, in particular, with respect to an increased need for methods of load alleviation to prolong fatigue life [Bottasso et al.(2013)Bottasso, Campagnolo, Croce, and Tib

Passive load alleviation through aeroelastic tailoring is attractive in its simplicity, design and is now well understood [Shirk et al.(1986)Shirk, Hertz, and Weisshaar].
It relies on a blade structure designed with bend-twist coupling (twist-towards-feather) to reduce the angle of attack as the blade bends upwards. This mod-

ifies aerodynamic loads, which can bring about positive effects on load alleviation. Numerical studies into the use of bend-twist coupling on wind turbine blades have shown that both fatigue load alleviation, of at least 20% (and up to 80%), and an equally significant reduction of maximum loads can be achieved [Lobitz and Veers(2003)]. When stability limits are considered, both flutter and divergence speeds are seen to drop, although they still occur well outside the operating regime. Furthermore, it has been demonstrated that the tailoring can be optimized such that the reduction in blade loads are achieved without penalties on performances, thereby reducing the cost of energy [Vesel Jr and McNamara(2014)].

Passive methods are quite limited to address effectively any arbitrary loading situations. Hence, active methods through pitch actuation has been proposed using feedback to reduced specific load components [Bossanyi(2003)]. Pitch control is seen to be the natural method for active load alleviation, given that this actuation already exists on modern wind turbines. Indeed, a recent study [Bottasso et al.(2013)Bottasso, Campagnolo, Croce, and Tibaldi] has explored the combined design of bend-twist coupled blades and individual pitch controls to bring about the full advantages of both mechanisms. As rotor size increases, individual pitch control may become less effective due to the large inertia and flexibility of the blades [Bergami and Henriksen(2012)]. Consequently, *smart rotor* concepts such as trailing-edge flaps, based on well-known aeronautical technology, have gained significant interest due to their rapid and localized load alleviation capabilities [Bergami and Poulsen(2014), Barlas and van Kuik(2010), Frederick et al.(2010)Frederick, Kerrigan, and Graham]. A summary of the most relevant studies in this area has already been presented in a recent paper by the authors [Ng et al.(2014)Ng, Hesse, Palacios, Graham, and Kerrigan] and it will not be repeated here.

In terms of modeling approaches, aeroservoelastic analysis requires the combination of structural and aerodynamic models, as well as an effective procedure to design control systems from them. Structural models based on composite beams provide an excellent balance between accuracy and effort for aeroelastic analysis and they have long been considered in most simulation environments [Hansen et al.(2006)Hansen, Sørensen, Voutsinas, Sørensen, and Madsen, Bottasso et al.(2013)Bottasso, Ca
Bergami and Henriksen(2012), Ng et al.(2014)Ng, Hesse, Palacios, Graham, and Kerrigan]. The common practice to modeling HAWT aerodynamics is through Blade-Element Momentum (BEM) theory. However, it has been shown that the accuracy of BEM deteriorates at high tip-speed-ratios (TSR) [Gupta and Leishman(2005)] and that BEM also over-predicts some critical loads such as root-bending moments (RBM) [Hauptmann et al.(2013)Hauptmann, Bülk, Erbslöh, Boorsma, Grasso, Kühn, and Cheng]. A higher-fidelity solution can be obtained using the time-domain Unsteady Vortex-Lattice Method (UVLM), which, under attached flow conditions, captures three-dimensional aerodynamic loads without the empirical corrections used in BEM [Voutsinas(2006), Leishman(2002)]. Moreover, UVLM-based aerodynamics can effectively be used for control design. Using this approach in Ref. [Ng et al.(2014)Ng, Hesse, Palacios, Graham, and Kerrigan], we demonstrated the use of trailing-edge flaps to reduce flapwise RBM and tip deflection on a single rotating blade subject to continuous turbulence. We investigated the trade-offs between RBM and torsion when using a single flap and further analyzed controller performance on nonlinear single blade models when structural deformations and aerodynamic influence coefficient matrices are re-computed at each

time instance. Methods of designing controllers from the full nonlinear turbine exist and they often require system identification [Castaignet et al.(2014)Castaignet, Barlas, Buhl, Poulsen, W Bergami and Poulsen(2014)] or different treatments of periodicity [Bottasso et al.(2014)Bottasso, Cacciola, an Geyler and Caselitz(2008), Ozdemir et al.(2011)Ozdemir, Seiler, and Balas, Lu et al.(2014)Lu, Bowyer, and On the other hand, single blade control models based on local measurements can be linearized and have been favoured for its simplicity and implementation [Larsen et al.(2005)Larsen, Madsen, and Thomsen, Leithead et al.(2009)Leithead, Neilson, Dominguez, Plumley et al.(2014)Plumley, Leithead, Jamieson, Bossanyi, and Graham]. This later approach will be followed in this work.

This paper investigates load alleviation strategies using blade-mounted flaps and aeroelastic tailoring on a full wind turbine with flexible tower and rotor. The composite beam finite-element model described in Ref. [Ng et al.(2014)Ng, Hesse, Palacios, Graham, and Ker will provide the basis to construct a flexible multi-body dynamics of the turbine, using Lagrange multipliers to include prescribed rotations between the tower and rotor. The aeroservoelastic methodology involving this multi-body structural dynamical model, unsteady vortex-lattice method and the coupled description will first be discussed in Section 3. Following which, numerical results are presented in Section 4, beginning with a short validation exercise on the implementation of the aeroelastic formulation on the NREL 5-MW wind turbine [Jonkman et al.(2009)Jonkman, Butterfield, Musial, and Scott]. We will then examine the effects of passive and active load alleviation and in particular, demonstrate the use of bend-twist coupling and flaps to reduce the root-mean-square (rms)/standard deviation of RBM, tip deflections and fatigue. While the separate use of passive mechanisms and active flap control for load alleviation have been well-studied, an integrated approach involving the two mechanisms has yet to be fully explored and will be investigated. We will also make comparisons between active flaps and pitch controls for load alleviation. The paper will then conclude with discussions on the key findings in Section 5.

3 Methodology

The aeroservoelastic modeling of HAWT is based upon an integrated framework developed for Simulation of High Aspect Ratio Planes (SHARP) [Palacios et al.(2010)Palacios, Murua, and Co Murua et al.(2012a)Murua, Palacios, and Graham, Hesse and Palacios(2012)], which has been adapted to model rotating blades [Ng et al.(2014)Ng, Hesse, Palacios, Graham, and Kerrigan]. The focus here will be initially on expanding the single-blade descriptions to full wind turbine models using concepts of flexible multi-body dynamics. A single-blade model will be then used to design a controller which is applied on the aeroelastic model of the full turbine.

3.1 Flexible Multi-body Dynamics Modeling of Rotor and Tower

The structural deformations of the tower and blades are represented by composite beams described in a moving frame of reference (FoR) [Simo and Vu-Quoc(1988), Géradin and Cardona(2001)]. We follow the structural model of Ref. [Hesse and Palacios(2012)], which accounts, in general, for large (geometrically-nonlinear) deformations. The actual structure in the three-dimensional space is first reduced to a one-dimensional representation using a methodology for cross-section analysis [Palacios and Cesnik(2005),

Dizy et al.(2013)Dizy, Palacios, and Phino]. The inclusion of tower dynamics in the modeling of large wind turbines defines a multi-body dynamics problem. Blades and tower are modeled using beam elements, with their structural dynamics described with respect to hub frame S and tower base frame A, respectively, as illustrated in Figure 1. Although not explored in this paper, the motion of frame A at the tower base is further described with respect to the inertia frame G to take into account of any platform motion found in floating structures.

The equations of motion describing the dynamics of a structural subcomponent i (i.e., the tower or a rotor blade) is expressed in residualized form as [Palacios et al.(2010)Palacios, Murua, and Cook, Géradin and Cardona(2001)]:

$$\boldsymbol{\mathcal{R}}\left(\boldsymbol{\eta}_i, \dot{\boldsymbol{\eta}}_i, \ddot{\boldsymbol{\eta}}_i, \boldsymbol{\nu}_i, \dot{\boldsymbol{\nu}}_i\right) = \boldsymbol{\mathcal{M}}\left(\boldsymbol{\eta}_i\right) \begin{Bmatrix} \ddot{\boldsymbol{\eta}}_i \\ \dot{\boldsymbol{\nu}}_i \end{Bmatrix} + \boldsymbol{Q}_{stif}\left(\boldsymbol{\eta}_i\right) + \boldsymbol{Q}_{gyr}\left(\boldsymbol{\eta}_i, \dot{\boldsymbol{\eta}}_i, \boldsymbol{\nu}_i\right) - \boldsymbol{Q}_{ext} = 0 \tag{1}$$

where $\boldsymbol{\mathcal{M}}$ is the discrete mass matrix, and $\boldsymbol{Q}_{stif}$, $\boldsymbol{Q}_{gyr}$ and $\boldsymbol{Q}_{ext}$ are the discrete elastic, gyroscopic and external generalized forces, respectively. The matrix $\boldsymbol{\eta}_i$ contains nodal displacements/rotations along subcomponent i, while $\boldsymbol{\nu}_i$ contains the corresponding rigid-body velocities (velocities of reference frame S for the blades and of reference frame A for the tower). In the multi-beam configuration of the rotor, three identical structures representing the blades (azimuthally spaced at 120° apart) are connected to the shaft, and rotational effects are prescribed through its base motions.

The velocities of frame S fixed to the rotor hub are now constrained, using Lagrange multipliers, to match the nodal velocities of the local frame B_t at the tower top and the rotor angular speed. The system of equations coupling the rotor and tower is augmented from Eq. (1) to form:

$$\begin{aligned} &\begin{Bmatrix} \boldsymbol{\mathcal{R}}_t \\ \boldsymbol{\mathcal{R}}_r \end{Bmatrix}\left(\boldsymbol{\eta}, \dot{\boldsymbol{\eta}}, \ddot{\boldsymbol{\eta}}, \boldsymbol{\nu}, \dot{\boldsymbol{\nu}}\right) + \boldsymbol{\Phi}_{nh}^{\top}\dot{\boldsymbol{\lambda}} + \boldsymbol{J}\boldsymbol{\lambda} = 0\,, \\ &\boldsymbol{\Phi}_{nh}\begin{Bmatrix} \dot{\boldsymbol{\eta}} \\ \boldsymbol{\nu} \end{Bmatrix} + \boldsymbol{\phi} = 0 \end{aligned} \tag{2}$$

where the subscripts t and r correspond to the tower and rotor blades, respectively. The structural and rigid-body degrees-of-freedom $\boldsymbol{\eta}$ and $\boldsymbol{\nu}$ now contain the structural and rigid-body contributions of all bodies, while $\boldsymbol{\lambda}$ are the Lagrange multipliers of the rotor/tower constraint. Eq. (2) provides the constrained flexible-body dynamics description, with $\boldsymbol{\Phi}_{nh}$ representing the nonholonomic quantity of all constraints and the vector $\boldsymbol{\phi}$ containing any prescribed velocities (in particular, the angular velocity of the rotor). Finally, $\boldsymbol{J}$ is the tangent matrix of all algebraic constraints between each pair of bodies, that is, $\boldsymbol{J}_{ij} \triangleq \partial\boldsymbol{\Phi}_{nh,ij}/\partial\boldsymbol{\eta}_i$.

The coupled wind turbine system in Eq. (2) can now be linearized around a

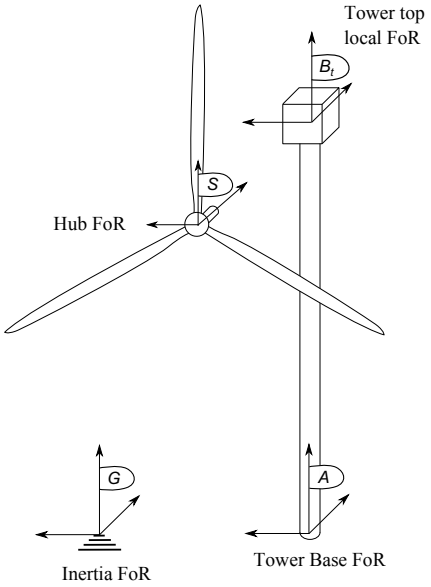

Figure 1: Multi-body configuration of the combined rotor and tower model including FoR definitions.

constant rotor velocity leading to:

$$\begin{bmatrix} \boldsymbol{\mathcal{M}}_t^{SS} & \mathbf{0} & \mathbf{0} & -\boldsymbol{\Lambda}^\top \\ \mathbf{0} & \boldsymbol{\mathcal{M}}_r^{SS} & \boldsymbol{\mathcal{M}}_r^{SR} & \mathbf{0} \\ \mathbf{0} & \boldsymbol{\mathcal{M}}_r^{RS} & \boldsymbol{\mathcal{M}}_r^{RR} & \boldsymbol{A}_{CC}^\top(\theta) \\ \mathbf{0} & \mathbf{0} & \mathbf{0} & \mathbf{0} \end{bmatrix} \begin{Bmatrix} \Delta\ddot{\boldsymbol{\eta}}_t \\ \Delta\ddot{\boldsymbol{\eta}}_r \\ \Delta\dot{\boldsymbol{\nu}}_r \\ \Delta\dot{\boldsymbol{\lambda}} \end{Bmatrix} + \begin{bmatrix} \boldsymbol{C}_t^{SS} & \mathbf{0} & \mathbf{0} & \mathbf{0} \\ \mathbf{0} & \boldsymbol{C}_r^{SS} & \boldsymbol{C}_r^{SR} & \mathbf{0} \\ \mathbf{0} & \boldsymbol{C}_r^{RS} & \boldsymbol{C}_r^{RR} & \mathbf{0} \\ \boldsymbol{\Lambda} & \mathbf{0} & -\boldsymbol{A}_{CC}(\theta) & \mathbf{0} \end{bmatrix} \begin{Bmatrix} \Delta\dot{\boldsymbol{\eta}}_t \\ \Delta\dot{\boldsymbol{\eta}}_r \\ \Delta\boldsymbol{\nu}_r \\ \Delta\boldsymbol{\lambda} \end{Bmatrix}$$
$$+ \begin{bmatrix} \boldsymbol{K}_t^{SS} & \mathbf{0} & \mathbf{0} & \mathbf{0} \\ \mathbf{0} & \boldsymbol{K}_r^{SS} & \mathbf{0} & \mathbf{0} \\ \mathbf{0} & \boldsymbol{K}_r^{RS} & \mathbf{0} & \mathbf{0} \\ \mathbf{0} & \mathbf{0} & \mathbf{0} & \mathbf{0} \end{bmatrix} \begin{Bmatrix} \Delta\boldsymbol{\eta}_t \\ \Delta\boldsymbol{\eta}_r \\ \mathbf{0} \\ \mathbf{0} \end{Bmatrix} = \begin{Bmatrix} \mathbf{0} \\ \boldsymbol{Q}_{ext} \\ \int \boldsymbol{Q}_{ext} \\ \mathbf{0} \end{Bmatrix} \tag{3}$$

with the superscripts S and R denoting structural and rigid-body contributions, respectively. In the above description, the rigid-body motion of the tower is removed in the land-based configuration of the HAWT. The transformation matrices $\boldsymbol{\Lambda}$ and $\boldsymbol{A}_{CC}$ enforce the velocity constraints between the rotor hub S and tower top frame B_t. The transformation $\boldsymbol{A}_{CC}$ further accounts for changes in orientation between the two frames due to rotation of the rotor. The prescribed rotor velocity and azimuth angles of the rotor blades at steady-state, Ω and $\theta = \Omega t$, respectively, lead to gyroscopic contributions to the damping as well as stiffness matrices with non negligible effects on the vibration characteristics of the coupled system [Ng et al.(2013)Ng, Hesse, Palacios, Graham, and Kerrigan]. The overall external forces and moments $\int \boldsymbol{Q}_{ext}$ acting at the rotor hub S are included in the third row of the equation to balance the forces due to the tower top motion $\boldsymbol{A}_{CC}^\top(t)\Delta\dot{\boldsymbol{\lambda}}$. Finally, the constraint function is included in the last

row of Eq. (3).

3.2 Unsteady Vortex-Lattice Method

The description for the aerodynamics is given by the discrete-time UVLM [Murua et al.(2012b)Murua, Palacio Katz and Plotkin(2001)] with a prescribed helicoidal wake [Chattot(2007)], providing a medium-fidelity representation of the unsteady aerodynamics in attached-flow conditions for arbitrary blade kinematics. As an extension to the single rotating blade [Ng et al.(2014)Ng, Hesse, Palacios, Graham, and Kerrigan], the non penetrating boundary condition now accounts for the interference due to circulations (both bound and wake) on the multiple blades of the rotor (but neglecting the aerodynamic interference with hub and tower):

$$\sum_{i=1}^{N}\left(\sum_{j=1}^{N}\left[\boldsymbol{A}_{b,ij}\boldsymbol{\Gamma}_{b,j}+\boldsymbol{A}_{w,ij}\boldsymbol{\Gamma}_{w,j}\right]+\boldsymbol{w}_i\right)=\boldsymbol{0} \tag{4}$$

In the above equation, N is the number of blades and the circulation strengths of the blade and wake vortex rings are given by $\boldsymbol{\Gamma}_b$ and $\boldsymbol{\Gamma}_w$, respectively. The aerodynamic influence coefficient matrices, $\boldsymbol{A}_b$ and $\boldsymbol{A}_w$, are obtained through the Biot-Savart law to account for the normal velocity induced on the lifting surface (blade). The downwash on the blade collocation points are represented by $\boldsymbol{w}$. The aerodynamic forces and moments are computed from the pressure distributions across panels on the blades through the unsteady Bernoulli equation [Katz and Plotkin(2001)]. Additional details can be found in Refs. [Ng et al.(2014)Ng, Hesse, Palacios, Graham, and Kerrigan, Murua et al.(2012a)Murua, Palacios, and

3.3 State-Space Aeroelastic Formulation

The structural dynamic equations of motion of the combined rotor and tower are discretized through the Newmark-β method [Géradin and Rixen(1997)]. The blades are subsequently coupled to the discrete-time UVLM using a coinciding spanwise panel discretization. In the fluid-structure coupling, aerodynamic loads at the center of each bound vortex ring's leading segment are mapped to their respective structural beam nodes. In turn, structural degrees-of-freedom (due to both blade elastic deformations and tower-top motions) are mapped as downwash on the blade collocation points. An illustration of the fluid-structure coupling in the aeroelastic model is shown in Figure 2. It includes disturbances due to either wind gusts or base motions, even though only the former will be considered in this study.

In the coupled model description, the structural beams representing the rotor blades are linearized around a prescribed rotational velocity, and nonlinearity enters the system through the constraints in Eq. (3), which is azimuth-dependent in the transformation matrix. Also, the tower injects an azimuth-dependent rigid-body downwash on the panel collocation points in the linear UVLM rotor description. The aeroelastic formulation accommodates for rotor asymmetry, such as imbalance, and also external asymmetric and time-varying loadings pertaining to operating conditions, such as wind shear, yaw error and gravity [Skjoldan(2011)].

With each bound and wake circulation in the UVLM model representing a state, the coupled equations of motion contain a large number of states and

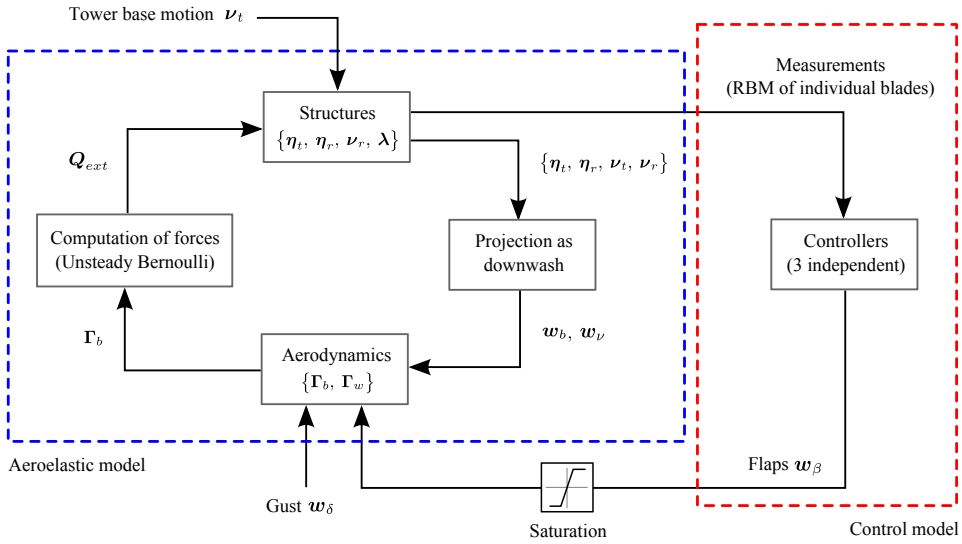

Figure 2: Fluid-structure coupling in the aeroelastic model and closed-loop configuration.

direct time-simulation easily becomes computationally prohibitive on a single-processor machine. Hence, the structural and UVLM models are reduced separately prior to coupling. This will also facilitate the synthesis of controllers for the coupled system. For the model reduction, firstly, the structural degrees of freedom are truncated using modal decomposition [Géradin and Rixen(1997)] on individual beams. Next, the UVLM model is reduced through balanced truncation, following the approach of Ref. [Hesse and Palacios(2014)], which showed that this is an effective approach in reducing large aeroelastic models.

From the coupled equations of motion of the UVLM and constrained structural model, we obtain the complete aeroservoelastic system in a time-varying discrete-time state-space form [Murua et al.(2012a)Murua, Palacios, and Graham], given by:

$$\begin{aligned} \boldsymbol{x}^{n+1} &= \boldsymbol{A}(\theta(t))\boldsymbol{x}^n + \boldsymbol{B}\boldsymbol{w}_\beta^n + \boldsymbol{G}\boldsymbol{w}_\delta^n \,, \\ \boldsymbol{y}^n &= \boldsymbol{C}\boldsymbol{x}^n + \boldsymbol{D}\boldsymbol{w}_\beta^n + \boldsymbol{H}\boldsymbol{w}_\delta^n \end{aligned} \tag{5}$$

where the state matrix $\boldsymbol{A}$ is a function of the azimuth angle $\theta(t)$, which defines the orientation of the rotor blades with respect to the tower at each time step n. The system is linear parameter-varying, but as $\theta = \Omega t$ is a function of time, the model becomes time-varying. The states are defined as:

$$\boldsymbol{x}^\top = \begin{bmatrix} \Delta\boldsymbol{\Gamma}_b^\top & \Delta\boldsymbol{\Gamma}_w^\top & | & \Delta\boldsymbol{\eta}_t^\top & \Delta\dot{\boldsymbol{\eta}}_t^\top & \Delta\boldsymbol{\eta}_r^\top & \Delta\dot{\boldsymbol{\eta}}_r^\top & | & \Delta\boldsymbol{\nu}^\top & \Delta\boldsymbol{\lambda}^\top \end{bmatrix} \tag{6}$$

containing the aerodynamics, structures and rigid-body states. The control input and external disturbance, $\boldsymbol{w}_\beta$ and $\boldsymbol{w}_\delta$, represent the additional downwash due flap deflection and gust, respectively. The output $\boldsymbol{y}$ contains measurements such as blade root loads, blade tip flapwise deflections and tower top out-of-plane deflections.

3.4 Control Model

In this study, the control model is based on the description of a single rotating blade with prescribed root motions. As nonlinearity in Eq. (5) stems from the dynamics of the tower in both the constrained structural equations of motion and the coupling terms with aerodynamics, this single rotating blade description (which is expressed in the rotating frame of reference) becomes linear time-invariant. The equations of motion have been described in Ref. [Ng et al.(2014)Ng, Hesse, Palacios, Graham, a and are written in the same state-space structure as in Eq. (5), but with a constant state matrix, that is:

$$\begin{aligned} \boldsymbol{x}_s^{n+1} &= \boldsymbol{A}_s \boldsymbol{x}_s^n + \boldsymbol{B}_s \boldsymbol{w}_{\beta,s}^n + \boldsymbol{G}_s \boldsymbol{w}_{\delta,s}^n \,, \\ \boldsymbol{y}_s^n &= \boldsymbol{C}_s \boldsymbol{x}_s^n + \boldsymbol{D}_s \boldsymbol{w}_{\beta,s}^n + \boldsymbol{H}_s \boldsymbol{w}_{\delta,s}^n \end{aligned} \tag{7}$$

where the subscript s denotes a single blade and the state vector contain only the aerodynamic and structural degrees-of-freedom pertaining to the single clamped rotating blade, that is, circulation on blade and wake vortex rings and nodal displacements and rotations along the blade elastic axis.

Here, $\mathcal{H}_\infty$ control design will be considered, which has been shown before to perform well for dynamic load alleviation [Barlas et al.(2013)Barlas, van Wingerden, Hulskamp, van Kuik, an Cook et al.(2013)Cook, Palacios, and Goulart] while providing robustness in wind turbine applications [Geyler and Caselitz(2008), Ozdemir et al.(2011)Ozdemir, Seiler, and Balas]. The objective of $\mathcal{H}_\infty$ control is to minimize the $\mathcal{L}_2$ gain of the linear fractional map $F(\boldsymbol{P}, \boldsymbol{K})$:

$$\| F(\boldsymbol{P}, \boldsymbol{K}) \|_\infty = \max_{\boldsymbol{w}_\delta \neq 0} \frac{\| \boldsymbol{z} \|_{\mathcal{L}_2}}{\| \boldsymbol{w}_{\delta,s} \|_{\mathcal{L}_2}} \tag{8}$$

with

$$\boldsymbol{z} = \begin{bmatrix} \boldsymbol{Q}^{\frac{1}{2}} & 0 \\ 0 & \boldsymbol{R}^{\frac{1}{2}} \end{bmatrix} \begin{bmatrix} \boldsymbol{y}_s \\ \boldsymbol{w}_{\beta,s} \end{bmatrix} \tag{9}$$

where $\boldsymbol{P}$ is the plant and $\boldsymbol{K}$ is the controller. The objective function $\boldsymbol{z}$ contains the weighted measurement $\boldsymbol{y}_s$ and control input $\boldsymbol{w}_{\beta,s}$ from Eq. (7). The $\mathcal{H}_\infty$ description signifies that the worst case response (in an $\mathcal{L}_2$ sense) of the system to the disturbance input is minimized [Skogestad and Postlethwaite(2005)]. Given that only root-bending-moments are measured for feedback and there is one flap on a single rotating blade of the control model, the weights $\boldsymbol{Q}$ and $\boldsymbol{R}$ in the objective function are scalers. In the selection of weights, the weight $\boldsymbol{Q}$ on the measurement output are increased relative to the control input weight $\boldsymbol{R}$ until the limits of flap deflection angle $|\beta| \leq 10°$ or rates $|\dot{\beta}| \leq 100°/\text{s}$ are encountered [Berg et al.(2009)Berg, Wilson, Resor, Barone, and Berg].

4 Numerical Results

The aeroelastic description outlined above is now used to model the NREL 5-MW reference wind turbine [Jonkman et al.(2009)Jonkman, Butterfield, Musial, and Scott]. Details of numerical implementation and validation will first be discussed, followed by an investigation on passive and active control methods for load alleviation.

4.1 NREL 5-MW Reference Wind Turbine

The tower and rotor blades, with properties from Ref. [Jonkman et al.(2009)Jonkman, Butterfield, Musial, an
are modeled as two-noded beam elements and connected through Lagrange multipliers. The nacelle and hub are modeled as point masses on the tower top at prescribed offset locations [Hansen et al.(2006)Hansen, Sørensen, Voutsinas, Sørensen, and Madsen]. A graphical representation of the NREL 5-MW turbine is shown in Figure 3, describing the locations and dimensions of various components [Jonkman et al.(2009)Jonkman, Butterfield, Mus

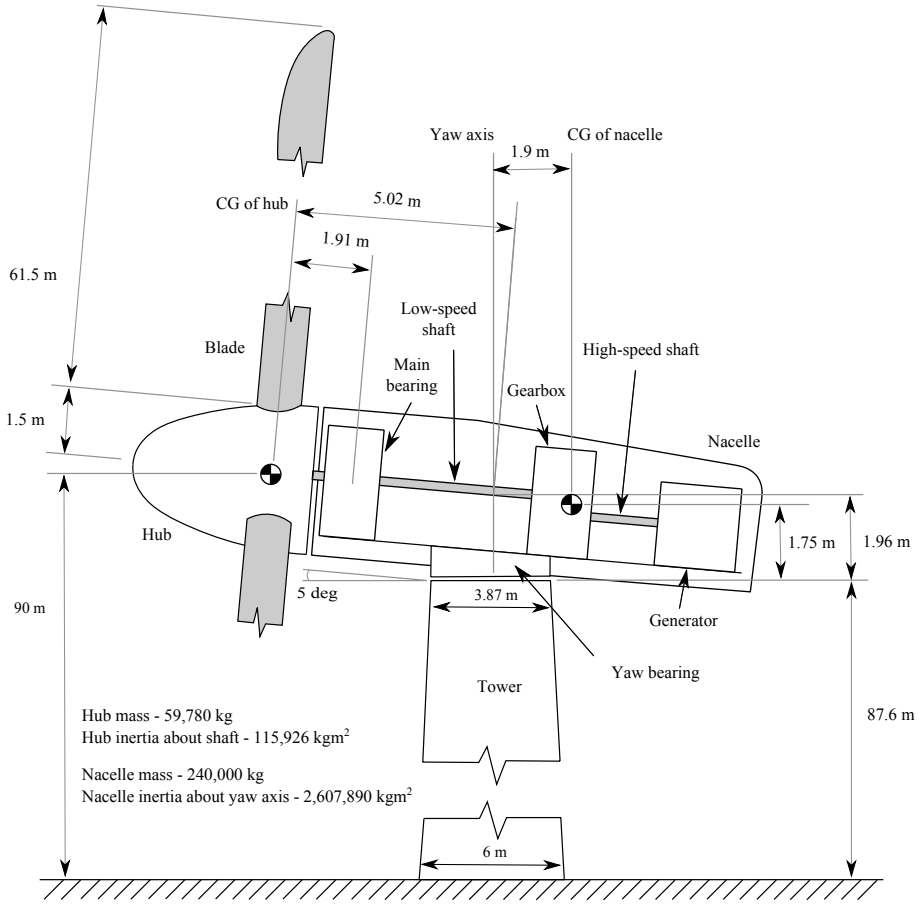

Figure 3: The NREL 5-MW wind turbine. The gearbox and generator are merged with the nacelle as a single point mass in the modeling, but are shown here for completeness.

For the aerodynamic model, the vortex panels are distributed in the outer 80% span of the turbine blade. In order to arrive at a linear UVLM description for computational efficiency, the wake profile is prescribed in a helicoidal shape [Chattot(2007)] defined by the inflow and rotational velocity, shown in Figure 4b. The difference in computing loads between a prescribed helicoidal wake against a free wake model has been shown to be marginal [Simoes and Graham(1992), Murua et al.(2012a)Murua, Palacios, and Graham]. Also, the flow along the

outer span of the blades, in particular the tip region where the flaps are located, operates in attached flow conditions [Bergami et al.(2014)Bergami, Riziotis, and Gaunaa]. The drag forces in the blade's inboard segment with circular cross-sections are neglected.

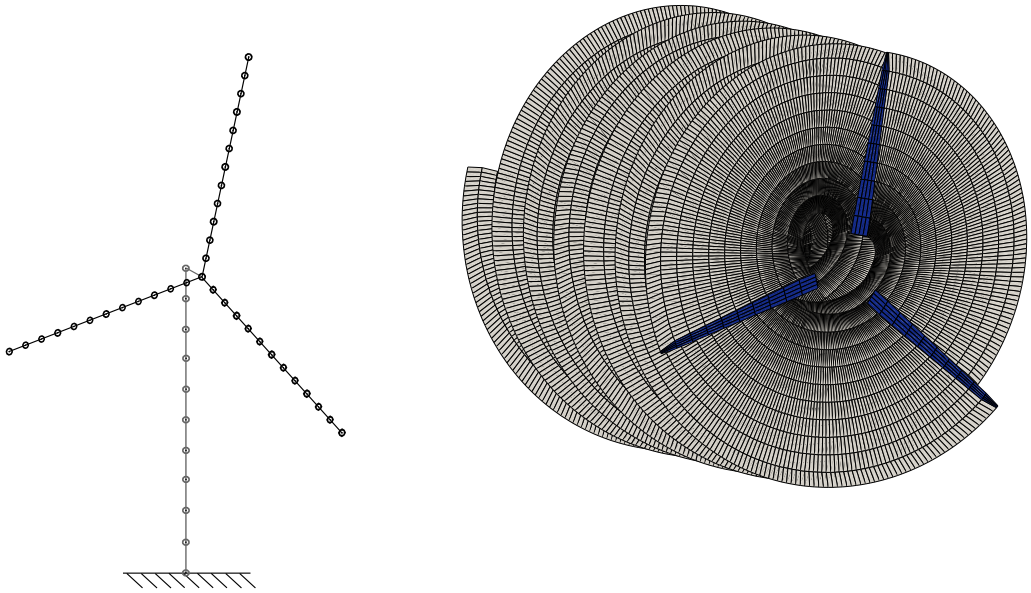

(a) Constrained multi-body configuration of the turbine.

(b) Aerodynamic model of rotor with prescribed helicoidal wake.

Figure 4: Aerodynamic and structural models used to represent the NREL turbine. (Four chordwise panels are used for visual clarity)

In the simulations that follow, the turbine is assumed to be operating at a rated 11 m/s inflow and TSR of 7. The wind field (gust) is in accordance to the International Electrotechnical Commission (IEC) standard [IEC 61400-1(2006)], and contains a turbulent wind field and wind shear described using a von Kármán spectrum and a power law of exponent 0.2, respectively. The open-source stochastic inflow turbulence tool, Turbsim [Jonkman and Kilcher()] by the U.S. National Renewable Energy Laboratory, is used to generate the wind field with grid size of 31×31. Each simulation is performed on 6×600 seconds of wind field with characteristic hub height turbulence intensity of 17.5%.

4.2 Validation and Numerical Implementation

The implementation of the aeroelastic description to model a single rotating blade has been performed in a previous study [Ng et al.(2014)Ng, Hesse, Palacios, Graham, and Kerrigan]. Progressing from the single rotating blade to the full rotor, we will first investi-

gate the effects of wake interactions on the aerodynamic loads resulting from the presence of multiple lifting surfaces. Next, the structural equations of motion are verified by matching the natural frequencies of the full wind turbine in parked conditions [Jonkman et al.(2009)Jonkman, Butterfield, Musial, and Scott], followed by a discussion on the numerical implementation.

Firstly, in modeling the rotor, the three NREL 5-MW blades are placed at 120° azimuth from each other with cross influence of circulation included in the UVLM model. The main effect of the multiple lifting surfaces is to generate additional backflow from the rotating wake (as in Eq. (4)), thus reducing loads on the blades. This is equivalent to the axial induction factor used in BEM theory [Hansen et al.(2006)Hansen, Sørensen, Voutsinas, Sørensen, and Madsen]. Figure 5 shows the normalized aerodynamic lift on one of the blades in the full rotor subject to an impulsively started flow and the vertical dotted lines indicate each time the blade have rotated 120°. It can be observed that in the transient stage, each time the blade passes through the wake shed by another blade or by itself, the aerodynamic loads are reduced. Also plotted on the same figure is a single rotating blade for comparison, showing a lower reduction in load when the blade passes by its own shed wake after a full rotation. In steady state, the loads in the full rotor configuration are about 15% lower than in a single rotating blade.

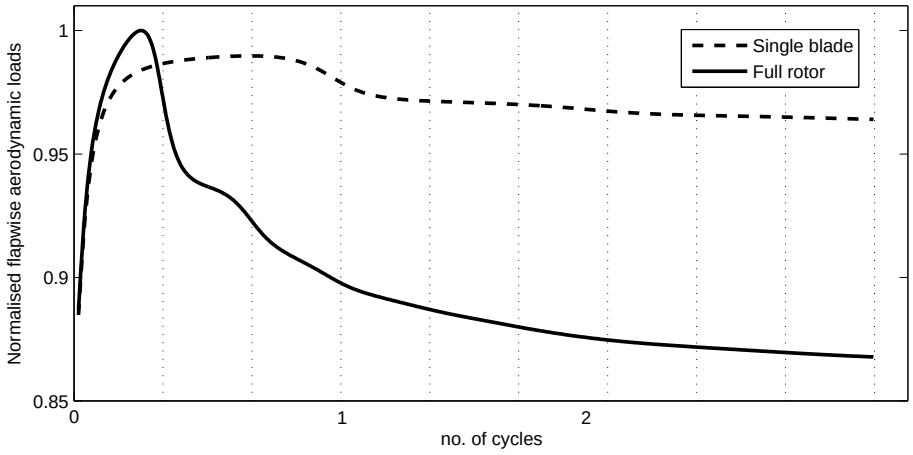

Figure 5: Instantaneous lift for a single rotating blade and for the full rigid rotor when subjected to an impulsively started gust. Results are normalized with respect to the maximum value. Vertical dotted lines indicate each time a blade have rotated 120°.

The effect of tower shadow on a turbine is accounted for in potential flow theory by a doublet array along the tower centerline [Burton(2011)]. For the NREL wind turbine, with 5° rotor pitch and assuming an undeformed configuration in rotation, the velocity deficit experienced by the blades due to tower shadow ranges between 0.15 to 0.07 from their root to tip. Even though the tower may have a larger circumference towards its base, the effect of blockage on the blades in this region is smaller than at the tower top due to the 5° pitch of the rotor. The tower shadow imposes 1P loads on the rotating blades, as it does in wind shear of a full wind field. In a parametric study not shown here,

the effects of tower shadow in the presence of a full wind field on the blade flapwise RBM were assessed and found to be insignificant, indicating that the 1P loads are dominated by wind shear and therefore they not included in the final model. However, tower shadow may become significant in cases of large blade deformations.

Next, the implementation of the HAWT structural equations of motion are verified. The natural frequencies of the turbine in parked configuration are computed using the same discretization as documented (10 tower elements and 48 elements for each of the blades). They are listed in the second last column of Table 1 and agree well with those obtained using FAST and ADAMS in Ref. [Jonkman et al.(2009)Jonkman, Butterfield, Musial, and Scott]. The corresponding mode shapes are shown in Figure 6.

Table 1: Computed natural frequencies (Hz) of the stationary NREL turbine for structural discretization of (a) 10 tower elements and 48 elements on each blade (10t, 48b), (b) 10 tower elements and 12 elements on each blade (10t, 12b) with interpolated blade properties. Comparison with FAST and ADAMS from Ref. [Jonkman et al.(2009)Jonkman, Butterfield, Musial, and Scott].

Mode	**Description**	**FAST**	**ADAMS**	**SHARP** (10t, 48b)	**SHARP** (10t, 12b)
1	1^{st} Tower Side-to-Side	0.312	0.316	0.315	0.316
2	1^{st} Tower Fore-Aft	0.324	0.320	0.320	0.321
3	1^{st} Drivetrain Torsion	0.621	0.609	0.611	0.617
4	1^{st} Blade Asymmetric Flapwise-Yaw	0.667	0.630	0.641	0.662
5	1^{st} Blade Asymmetric Flapwise-Pitch	0.668	0.669	0.670	0.693
6	1^{st} Blade Collective Flap	0.699	0.701	0.703	0.726
7	1^{st} Blade Asymmetric Edgewise-Pitch	1.08	1.07	1.08	1.09
8	1^{st} Blade Asymmetric Edgewise-Yaw	1.09	1.09	1.10	1.11
9	2^{nd} Blade Asymmetric Flapwise-Yaw	1.93	1.65	1.73	1.79
10	2^{nd} Blade Asymmetric Flapwise-Pitch	1.92	1.86	1.88	1.96
11	2^{nd} Blade Collective Flap	2.02	1.96	1.97	2.06
12	2^{nd} Tower Fore-Aft	2.90	2.86	2.91	2.93
13	2^{nd} Tower Side-to-Side	2.94	2.94	3.03	3.04

The convergence of UVLM relies on the panel discretization in both the blades and wakes. In particular, the length of the wake determines the ability to capture unsteadiness in the aerodynamics and wake interaction among the blades. Through a panel discretization convergence study, it was seen that an equally distributed 10 spanwise and 20 chordwise panels in the blade, with a wake profile of a quarter rotor diameter downstream is sufficient to represent the rotor and flap dynamics.

The one-dimensional finite-element discretization of the structure coincides with the spanwise panel discretization of the UVLM in Figure 4a. Including the inner span of the blade with cylindrical cross section in the structural beam model, and maintaining regular discretization, a total of 12 elements for each blade is used. The characteristics of the blade are obtained using a linear interpolation on the documented structural properties [Jonkman et al.(2009)Jonkman, Butterfield, Musial, and Sc which had 48 elements for the blades. The natural frequencies for the turbine

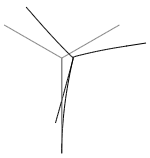

(a) 1st Tw SS (0.315 Hz)

(b) 1st Tw FA (0.320 Hz)

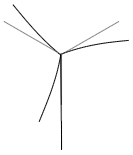

(c) 1st DT Tor (0.611 Hz)

(d) 1st Blade Asym FY (0.641 Hz)

(e) 1st Blade Asym FP (0.670 Hz)

(f) 1st Blade Coll Flap (0.703 Hz)

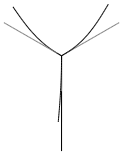

(g) 1st Blade Asym EP (1.08 Hz)

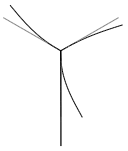

(h) 1st Blade Asym EY (1.10 Hz)

(i) 2nd Blade Asym FY (1.73 Hz)

(j) 2nd Blade Asym FP (1.88 Hz)

(k) 2nd Blade Coll Flap (1.97 Hz)

Figure 6: Stationary mode shapes of the NREL turbine in parked configuration. The abbreviations are: Tw (Tower), SS (Side-Side), FA (Fore-Aft), DT (Drivetrain), Tor (Torsion), Asym (Asymmetric), FY (Flapwise-Yaw), FP (Flapwise-Pitch), Coll (Collective), EP (Edgewise-Pitch), EY (Edgewise-Yaw).

with 12 elements on each blade and 10 tower elements are listed in the last column of Table 1, showing only a marginal differences from the baseline model. The resulting coupled aeroelastic system (5), using this discretization contains a total of just over 30,000 states.

The reduction of the structural model through modal decomposition is achieved through a parametric study on the full aeroelastic system suggesting that it is sufficient to keep only the lowest 10 tower modes and 140 blades modes. This was carried out by looking at the frequency response on snapshots of Eq. (5) at various instantaneous azimuth values of θ.

As an illustration, we consider the case of setting $\theta = 0^\circ$ and analyze the Bode diagram from gust input to various outputs on one of the blades. As shown in Figure 7a, the dominant low frequency dynamics for blade flapwise RBM can be captured relatively well using just 60 of the lowest rotor modes. However, this is insufficient for blade root torsion in Figure 7b where we will need at least 140 rotor modes to match the amplitude. The reason is that

for torsion, the superposition of higher frequency mode shapes are essential in obtaining the resulting quasi-static torsional amplitudes that are crucial in fluid-structure mapping. It should also be noted that the rise in torsional gain with frequency is due to the location of the elastic axis at quarter chord, resulting in moments being dominated by non-circulatory lift from the perspective of classical unsteady aerodynamics solution. As frequency increases further (beyond the range plotted), the magnitude eventually falls off due to structural damping.

As the modal truncation here is based on a frequency cut-off of the lowest 140 rotor modes, it unavoidably also retains a considerable amount of high frequency modes that do not contribute to the blade torsion. However, this is still preferred as it provides a robust procedure to describe the structural dynamics. Note also that, in the above cases, all tower modes are kept. A further study in Figure 8 identified that actually only 10 tower modes are needed to capture the tower fore-aft deflection.

The reduction of the unsteady aerodynamics is performance using balanced truncation. The Hankel Singular Values (HSV) [Skogestad and Postlethwaite(2005)] of the balanced UVLM model with respect to the largest HSV are shown in Figure 9. HSV provide a measure of the energy contribution of each state to the input/output behavior of the system and, in the current balanced UVLM model, relative states that are smaller than three orders of magnitude are truncated. The reduced UVLM model is then coupled with the truncated structural equations and simulated using turbulent input signals. The time marching solutions compared well with the full system, providing confidence that the reduced UVLM model retains key dynamical characteristics of the full aeroelastic model. We have analyzed the solution of the truncated UVLM in the fully coupled system to avoid truncating states that appear insignificant in the aerodynamics model but may still be crucial in the coupling process. Similar to modal truncation, Bode plots from gust input to RBM and torsion are shown in Figure 10 and it is evident that the reduced model of keeping 350 aerodynamic states, 10 tower modes and 140 blade structural modes is able to capture dominant lower frequency responses for blade flapwise RBM and root torsion. The full model in the figure has all the structural modes and aerodynamic states.

As a result, the reduced aeroelastic model for simulation has close to 900 states. Moreover, with the rotor blades returning to the same azimuth location after each round of rotation, all the state matrices in the first rotation can be stored and extracted for use in subsequent loops. The simulation is time-marched at 28.5Hz. These methods, including model reductions in the structures and aerodynamics as described, help to save computation time by more than two orders of magnitude with minimal impact on the accuracy of the simulations. More aggressive reductions in size would be possible for controller design, but it was not deemed necessary for the purpose of this work.

Instead of reducing the structures and aerodynamics separately before coupling, an alternative is to define and reduce the aeroelastic description of the rotor prior to coupling with the tower structural dynamics. As nonlinearity in the complete turbine stems from the tower, the aeroelastic description of the rotor alone is given by a linear time-invariant system. By reducing the rotor as a whole, the fluid-structure mapping is preserved within the aeroelastic model, and model reduction can be performed using less input/output channels defined by the overall simulation, hence requiring less states to be retained. An investigation was carried out to assess this and it was found that the number of states

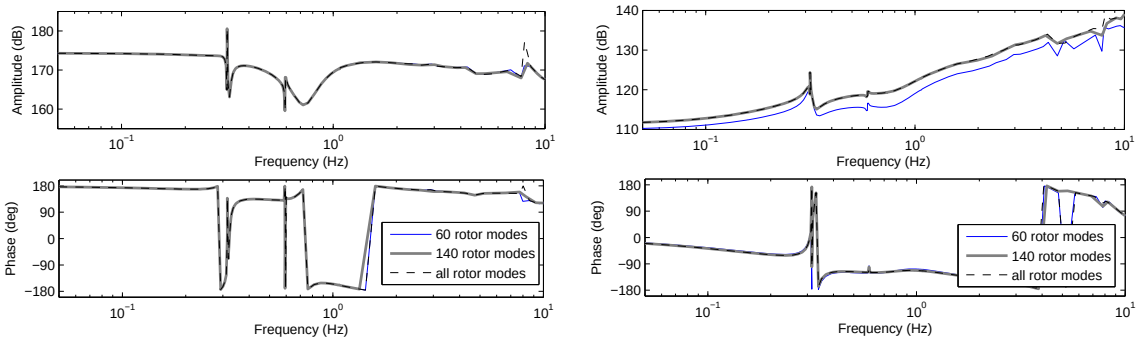

(a) Gust input to blade flapwise RBM.

(b) Gust input to blade root torsion.

Figure 7: Bode plot from gust input to flapwise RBM and root torsion on one of the rotor blades at an instantaneous azimuth angle $\theta = 0°$. Comparing the effects of truncating structural modes on rotor by keeping the lowest (i) 60 rotor modes, (ii) 140 rotor modes and (iii) all rotor modes. In the above cases, all tower structural modes and aerodynamic states are kept.

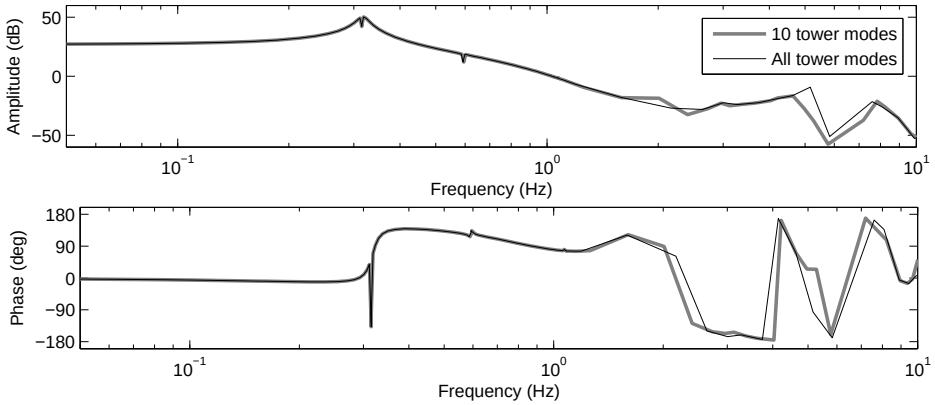

Figure 8: Bode plot from gust input to tower top fore-aft deflection. Comparing the effects of truncating structural modes on tower by keeping the lowest (i) 10 tower modes, (ii) all tower modes. In the above cases, 140 rotor modes and all aerodynamic states are kept.

required to capture the dynamics without affecting accuracy is still relatively large (at least 500 states) and not much smaller than the separate reduction of structural and aerodynamic modules. As the split procedure provides a better insight into the system dynamics, results are presented using that approach.

4.3 Passive Load Alleviation

Fiber-reinforced plastics are characterized by anisotropic behavior and can be used to tailor the elastic response of the structure [Hodges and Pierce(2002)]. For wind turbine blades where bending is the dominant load, coupling be-

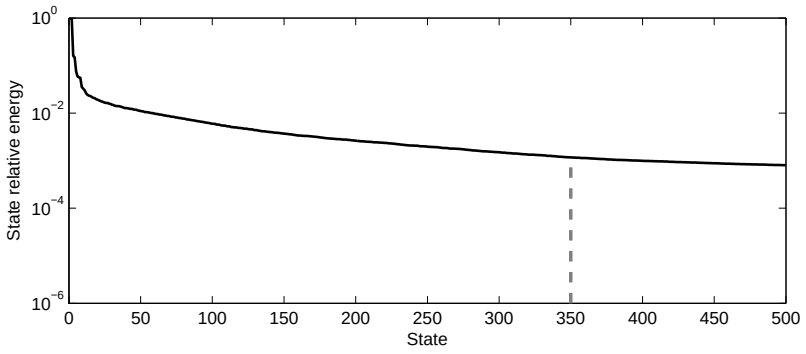

Figure 9: Normalized Hankel Singular Values of the balanced UVLM model with respect to the largest HSV.

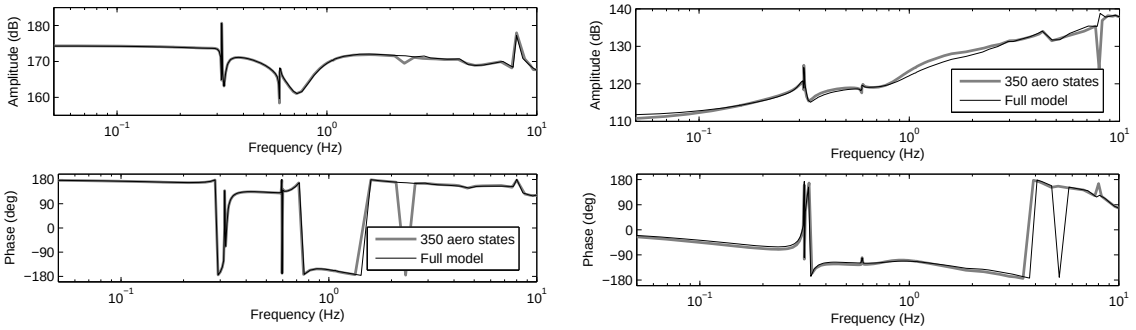

(a) Gust input to blade flapwise RBM.

(b) Gust input to blade root torsion.

Figure 10: Bode plot from gust input to blade flapwise RBM and root torsion on one of the rotor blades at an instantaneous azimuth angle $\theta = 0°$. Comparing the effect of keeping 350 aerodynamic states (with 10 tower and 140 rotor structural modes). Full model has all structural modes and aerodynamic states.

tween flapwise bending and torsion have shown to be beneficial for load alleviation [Lobitz and Veers(2003)]. If EI is the bending stiffness and GJ is the torsional stiffness, bend-twist coupling can be introduced to the linearized beam equation through an off-diagonal term in the sectional stiffness matrix. This bend-twist coupling will be defined as $\alpha\sqrt{GJ \times EI}$, with $-1 < \alpha < 1$ [Hodges and Pierce(2002)]. To simplify comparisons, we assume that the values of EI and GJ are kept constant. However, in actual practice, when fibers are oriented away from their principal axes, the stiffness values in the original directions will be lower, unless more fiber plies are added.

To begin, consider a single rotating NREL blade, the aeroelastic stability plot for varying amounts of elastic coupling is shown in Figure 11. For ease of visualization, the stability plot is separated into the negative and positive elastic couplings. With increasing negative coupling (twist-towards-feather) from 0.0 to -0.8 in Figure 11a, the torsional and first flapwise modes become less damped as their roots are shifted to the right. The fourth flap mode (with significant

torsion) moves down with increasing negative coupling, indicating that higher frequency flap/torsion modes are more easily excited. Due to the structural pre-twist in the blade, edgewise modes are also affected through the flapwise bending component in the coupling. These trends indicate that even though twist-to-feather is beneficial to load alleviation, it comes at the cost of increased excitation of higher frequency modes in the elastically coupled blades.

The root locus for varying α from 0.0 to 0.5 is shown in Figure 11b. With increasing positive coupling (twist-towards-stall), the torsional mode shifts to the right and approaches the fourth flap mode, with potential interaction. The first flapwise mode becomes highly damped and the edgewise modes are left relatively stagnant, except for the second edge that becomes more damped. As α is increased to 0.5, one of the real aerodynamic roots becomes positive, indicating instability through divergence.

The effect of elastic coupling on passive load alleviation on the full wind turbine is demonstrated in Figure 12. The values of blade RBM, torsion and tower fore-aft deflection are averaged across six turbulence seeds and normalized against their respective rms values at $\alpha = 0$. Note that rms values and standard deviation are the same when zero mean is used. With twist-towards-feather, the rms of RBM is reduced significantly and is almost halved with large amounts of negative coupling. Even though there is an accompanying rise in rms of torsion, the increase is relatively moderate. On the other hand, with positive elastic coupling, both the rms of RBM and torsion increase very quickly as a result of twist-towards-stall.

4.4 Active Load Alleviation

Next, the turbine is fitted with one flap on each blade to investigate their effectiveness in load reduction. Based on a previous numerical investigation [Ng et al.(2013)Ng, Hesse, Palacios, G the selected trailing-edge flap occupies the location from 70% to 90% span and measures 10% of local chord.

The controller is synthesized from a single NREL blade in a clamped configuration that is described in a rotating frame and written in linear time-invariant state-space representation (See Section 3.4). The chordwise UVLM discretization of the control model is the same as the discretization on the rotor blades of the full turbine model to enable the same time step in the discrete-time $\mathcal{H}_\infty$ controller. The number of spanwise and wake panels in the control model is also the same as those on the rotor blades. When the controller is connected to the full turbine model, a decentralized system is formed in which three independent controllers act on the flaps on the three blades. The feedback to the controllers is selected to be the flapwise RBM of the individual blades (See Figure 2). As mentioned for the $\mathcal{H}_\infty$ formulation, the weights on the states (measurement output) are increased with respect to the control inputs (deflection angle of the flap β) until the limits of $|\beta| \leq 10^\circ$ or $|\dot{\beta}| \leq 100^\circ/\text{s}$ are encountered [Berg et al.(2009)Berg, Wilson, Resor, Barone, and Berg] in a characteristic operating condition. Details are found in Ref. [Ng et al.(2014)Ng, Hesse, Palacios, Graham, and Kerrigan] and the resulting controller contains 50 states.

In closed-loop, we observe 13% rms reduction in blade flapwise RBM on the reference turbine, as shown in Table 2 for the six turbulence seeds. There is also a positive effect on reducing stationary component loads such as the tower fore-aft deflection. However, there is a significant increase in torsion as a result of ad-

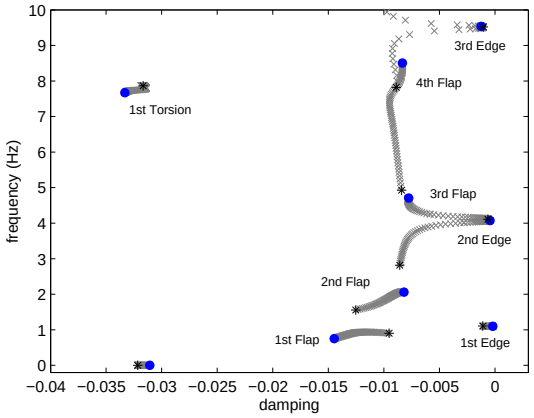

(a) Twist-towards-feather with negative elastic coupling parameter varied from $\alpha = 0.0$ (blue circle) to $\alpha = -0.8$ (black star).

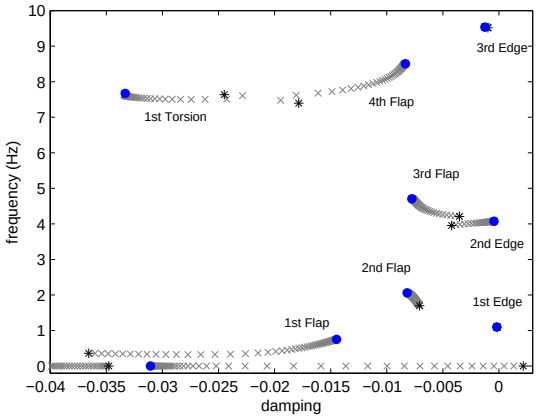

(b) Twist-towards-stall with positive elastic coupling parameter varied from $\alpha = 0.0$ (blue circle) to $\alpha = 0.5$ (black star).

Figure 11: Root locus of the NREL blade for varying degrees of elastic coupling.

ditional moments about the elastic axis that are generated by the flap deflections (negative percentage reductions in the table). This can be overcome by including torsion in the objective function of the controller to be minimized, as demonstrated in [Ng et al.(2014)Ng, Hesse, Palacios, Graham, and Kerrigan] but not explored here. For the fatigue analysis [Freebury and Musial(2000), Hendriks and Bulder(1995), Hayman()], an S-N slope of 10, typical for composite materials is chosen. The tabulated results consider only the time-series of the RBM from the simulation without weighting of wind speeds. Hence, the average Damage Equivalent Load (DEL) reduction of around 13% here, is used as an estimate of the fatigue loads.

A section of the measurement time-series on one of the three blades in operation is shown in Figure 13. Comparing the open-loop and closed-loop responses for blade RBM and tip deflection in Figures 13a and 13c, respectively, it is ap-

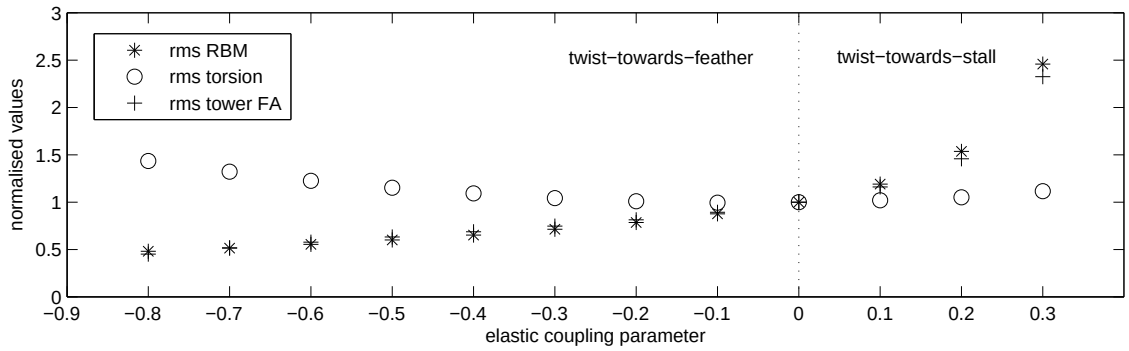

Figure 12: Open-loop blade RBM, torsion and tower fore-aft deflection with varying degrees of elastic coupling. Results are averaged across six turbulence seeds and normalized against their respective rms values at $\alpha = 0$.

Table 2: Closed-loop performance using active flap controls across six different turbulence seeds. Negative sign implies an increase. Operating condition are under 11m/s inflow, TSR of 7 and 17.5% turbulence intensity.

% reduction rms RBM	12.9 ± 0.1	% reduction max blade tip deflection	16.0 ± 2.2
% reduction rms torsion	-97.9 ± 5.3	% reduction rms tower fore-aft deflection	11.1 ± 0.2
% reduction max RBM	12.6 ± 0.6	max β (°)	9.01 ± 0.99
% reduction max torsion	-84.4 ± 17.2	max $\dot{\beta}$ (°/s)	34.9 ± 2.6
% reduction DEL RBM	13.3 ± 0.89		

parent that important reductions are present in the deterministic 1P loads. Yet, when the Power-Spectral-Density (PSD) of the RBM is plotted in Figure 14, the reduction is observed across most of the dominant frequencies. The PSD is computed using Welch's method to smoothen the power spectrum using eight segments of 50% overlap [Welch(1967)].

If specific frequency regions are to be targeted, low, high or band-pass filters can be included in the control input or measurement output signal [Barlas et al.(2012)Barlas, van der Veen, an Castaignet et al.(2013)Castaignet, Couchman, Poulsen, Buhl, and Wedel-Heinen]. In a parametric study, it was shown that if the controller is designed to act on a low-pass filtered measurement signal with cut-off frequency of 0.4Hz (2P), the reduction in rms, maximum and DEL values was 12.9%. This is almost similar to the case without filtering and yet, it required only half the amount of actuator duty if maximum $\dot{\beta}$ is taken to be the indicator. This indicates that loads in the lower end of the frequency spectrum are the main contributors to fatigue. For the bandwidth reduction, a second order Butterworth filter was used [Barlas et al.(2012)Barlas, van der Veen, and van Kuik].

In the full wind turbine model, saturation limits are placed on β and $\dot{\beta}$ (equivalent to the saturation block in Figure 2). Even though the controller is synthesized from a single rotating blade, it performed well with the full turbine model. However, β seldom reached the maximum limit of $|\beta| \leq 10°$ (see Table 2), and the maximum value of $\dot{\beta}$ was less than half that of the limit of $|\dot{\beta}| \leq 100°/s$. In an effort to improve performance that could potentially be

achieved through higher flap deflection angles and rates, the controller from the single blade was tuned such that the limits on β were exceeded. When implemented on the full turbine model (Figure 15), the saturation on β at $\pm 10^\circ$ was activated using controllers tuned to $|\beta| \leq 30^\circ$. The closed-loop results are shown in Table 3. It is clear that rms of flapwise RBM can be increased to over 30% using a more aggressive controller. While the limit on β is met, $\dot{\beta}$ was continuously increasing before saturating (100°/s) and leveling out. However, accompanying this is a large increase in rms torsion, which may outweigh the potential benefits in rms RBM. For the maximum values (RBM and blade tip deflection), the percentage reductions were less substantial, indicating that maximum values are more affected by the bounds on β. On the other hand, rms values are bounded by $\dot{\beta}$ limits. The improvement in fatigue follows the same trend as maximum RBM. The PSD for the closed-loop RBM is included in Figure 14 for controller tuned to $|\beta| \leq 30^\circ$, showing a further reduction across most frequencies compared to the default case of $|\beta| \leq 10^\circ$ tuned controller.

Table 3: Closed-loop performance using different controllers with tuning on maximum $|\beta|$ varied from 10° to 35°. For percentages, they are averaged across six turbulence seeds and for $\dot{\beta}$, the maximum values among the seeds are shown. The abbreviations are: rd (reduction), bl (blade), tw (tower), FA (Fore-Aft), defl (deflection). Operating condition are under 11m/s inflow, TSR of 7 and 17.5% turbulence intensity.

Controller tuning	**% rd rms RBM**	**% rd rms torsion**	**% rd max RBM**	**% rd max torsion**	**% rd DEL RBM**	**% rd max bl tip defl**	**% rd rms tw FA defl**
10°	13.0	-97.9	12.6	-84.4	13.3	16.0	11.1
12°	15.9	-127	14.5	-104	15.4	18.6	13.6
15°	19.6	-165	15.5	-115	16.5	20.3	16.7
20°	24.8	-222	16.2	-123	17.3	20.7	21.1
25°	28.6	-268	16.3	-126	17.6	20.6	24.3
30°	31.1	-304	16.4	-127	17.7	20.4	26.5
35°	32.1	-331	16.3	-127	17.5	19.1	27.4

The previous study has been based on 'lift flaps' in which a downward deflection of the flap generates aerodynamic lift that is in the opposite direction. A question arose as to whether 'moment flaps' could be beneficial in the context of the NREL blade. In 'moment flaps', such as those used in helicopter vibration control [Hodges and Pierce(2002), Chopra and Sirohi(2014)], the change in aerodynamic lift is in the same direction as flap deflection, as a result of the twisting of the blade created by the flap moments. This normally occurs when the blade is highly-flexible in torsion, such that the moments created about the elastic-axis due to flap deflection results in large changes in angle-of-attack, thereby generating additional lift that overshadows the effect of the flap. There is also the advantage of weight reduction in the blade. To investigate, the torsional stiffness of the NREL blade is reduced from its nominal value and the corresponding aeroelastic stability plot is shown in Figure 16. A single rotating blade is considered here as the focus is to analyze the use of 'moment flaps' as a concept and if feasible, apply on the complete turbine. As expected, torsional frequency falls with reduced torsional stiffness, and each time it bypasses a flap

mode, it gets 'repelled' slightly until it encounters the first flap mode and the aeroelastic system becomes unstable. Before that, we observe a rise in damping of the flapwise modes as torsional stiffness is reduced, which could be beneficial in reducing flapwise fatigue loads. The edgewise modes which have the least damping are also slightly more damped. Note that the mass of the blade is assumed to remain constant.

From the bode plot of gust input to blade flapwise RBM in Figure 17, control reversal is observed to occur between 40% to 30% of the original torsional stiffness (where the phase undergoes a 180° change at low frequencies). The closed-loop performance using an $\mathcal{H}_\infty$ controller subject to six turbulence seeds is shown in Figure 18. Here, a different controller is designed for each value of reduced torsional stiffness. As torsional stiffness is reduced, the closed-loop performance falls due to moments created by the flap that modifies the angle-of-attack of the blade. Performance reaches a minimum at around 30% torsional stiffness (control reversal point) and then rises sharply. Also plotted on the same figure are the rms values of RBM and torsion, which increases at an exponential rate as torsional stiffness is reduced. To conclude, it is clear that with the NREL blade, 'moment flaps' are not a possible solution given the large reduction in torsional stiffness required before aeroelastic amplification on the control input is observed.

4.5 Combined Passive and Active Load Alleviation

In the last two sections, bend-twist coupling and flap control have separately demonstrated potential in load alleviation on the turbine, raising the question of any synergies that can be derived from integrating the two mechanisms. This is achieved by attaching flaps to an elastically coupled blade, providing a combination of active and passive load alleviation capabilities. Table 4 shows the load reduction performances for varying degrees of elastic coupling (for α between -0.5 to 0.3 at intervals of 0.1). Performances without parenthesis are closed-loop percentage reductions by the action of active flaps alone on top of the reductions delivered by bend-twist coupling. Percentage reductions in parenthesis are for the combined action of active flap control and bend-twist coupling.

We observe that when active flaps are used, percentage reductions in rms and maximum RBM decrease with negative coupling despite an increased use of $\dot{\beta}$. This is likely due to the lower damping of the dominant first flapwise mode in Figure 11a, rendering the blade more flexible in the out-of-plane direction. However, when the closed-loop RBM values of the combined active flap with bend-twist coupling are compared against an uncoupled blade in open-loop (percentages in parenthesis), the combined load reductions are very significant. Flapwise RBM are reduced almost by half, and the corresponding percentage increase in torsional loads are kept relatively unchanged.

The trend is completely reversed with positive elastic coupling where we observe larger reductions in loads from active flap controls due mainly to the increased damping of the dominant first flapwise mode in Figure 11b. However, this larger reduction in loads brought about by the active flaps is insufficient to overcome the increase in loads due to the twist-to-stall action of the elastic coupling, resulting in negative load reductions (percentages in parenthesis). In all the cases considered, a different controller is designed for each value of elastic

coupling. In Table 4, the performances in percentages are averaged across six turbulence seeds, while the values of $\dot{\beta}$ are the maximum values across the seeds.

As an illustration, consider the case of α = -0.4, the twist-towards-feather effect reduces open-loop rms and maximum values of RBM by around 35% and 30%, respectively. Adding active flaps to this configuration adds a further 10% reduction, and despite having a larger $\dot{\beta}$, this relative reduction is still lower than the 13% in the uncoupled case. The combined effect of the two mechanisms is able to deliver about 40% load reduction when compared to an uncoupled blade with relatively small changes in the closed-loop torsional loads. When it comes to fatigue (DEL), it follows similar trends as the maximum values.

Table 4: Closed-loop performance with different degrees of bend-twist coupling. Note that the percentage reductions without parenthesis are the additional reductions due to flaps on top of the reductions delivered by the individually bend-twist coupled blades. The percentage reductions in parenthesis (*total*) represent the performance of combined active flap control and bend-twist coupling. Operating condition are under 11m/s inflow, TSR of 7 and 17.5% turbulence intensity.

a	**OL rms RBM (Nm)**	**OL rms torsion (Nm)**	**% rd rms RBM (*total*)**	**% rd rms torsion (*total*)**	**% rd max RBM (*total*)**	**% rd max torsion (*total*)**	**% r RB**
0.3	3.10×10^6	2.75×10^3	19.0 (*-98.5)*	-104 (*-130)*	18.1 (*-88.5)*	-80.2 (*-113)*	19.0
0.2	1.94×10^6	2.57×10^3	15.8 (*-29.3)*	-100 (*-111)*	14.9 (*-25.1)*	-80.8 (*-93.2)*	15.7
0.1	1.44×10^6	2.46×10^3	13.7 (*1.82)*	-96.2 (*-98.2)*	12.8 (*4.28)*	-77.4 (*-81.0)*	14.1
0.0	1.26×10^6	2.43×10^3	13.0 (*13.0)*	-97.9 (*-97.9)*	12.6 (*12.6)*	-84.4 (*-84.4)*	13.2
-0.1	1.11×10^6	2.41×10^3	12.3 (*23.2)*	-100 (*-98.4)*	11.8 (*21.7)*	-88.4 (*-85.8)*	12.5
-0.2	9.93×10^5	2.41×10^3	11.5 (*30.5)*	-102 (*-100)*	11.2 (*28.6)*	-90.9 (*-86.7)*	11.5
-0.3	9.02×10^5	2.42×10^3	10.8 (*36.4)*	-106 (*-105)*	10.7 (*34.2)*	-95.6 (*-91.0)*	11.4
-0.4	8.26×10^5	2.43×10^3	9.89 (*41.1)*	-105 (*-105)*	9.74 (*38.6)*	-97.2 (*-91.7)*	10.3
-0.5	7.60×10^5	2.45×10^3	8.93 (*45.3)*	-105 (*-106)*	8.55 (*42.6)*	-98.4 (*-93.3)*	9.07

Looking at the PSD of RBM for the coupled case of α = -0.4, we see in Figure 19 that the effect of the elastic coupling is focused on the lower frequency loads (3P and below), but amplifies the higher frequencies. This amplification of higher frequency loads is also observed when we analyzed the stability plot of a single blade in Figure 11a. When the flaps are actuated, the attenuation is in the higher frequency range, which also happens to be the region where elastic coupling had the loads amplified. As it can be seen, the flaps are capable of bringing the high frequency loads back to values similar to the uncoupled case. This is in contrast to the action of the flaps in the uncoupled blade which acted on all frequencies in Figure 19. It also explains why $\dot{\beta}$ increases in cases of twist-to-feather blades (negative coupling) in Table 4.

4.6 Comparison with Individual and Cyclic Pitch Controls

To provide a comprehensive comparison of methods to load alleviation for wind turbines and demonstrate the flexibility of the current aeroservoelastic model, pitch controls will now be briefly discussed [Henriksen et al.(2013)Henriksen, Bergami, and Andersen,

Wilson et al.(2009)Wilson, Berg, Resor, Barone, and Berg]. Pitch actuators currently exist on wind turbines and with simple re-design, can also be used to tackle blade loads [Bossanyi(2003)]. Using the same aeroelastic model described in previous sections, individual pitch controls (IPC) are modeled by imposing additional downwash on all the panels of the linearized UVLM model to account for changes in angle-of-attack from blade pitch. The controller for IPC is designed on a single rotating NREL blade, tuned to the pitch rate limits of $\pm 8°/s$ [Jonkman et al.(2009)Jonkman, Butterfield, Musial, and Scott], and subsequently connected to the full wind turbine with RBM feedback control. As mentioned, this forms a decentralized system in which three independent controllers act on the pitch mechanism of the three blades. The overall configuration is similar to Figure 2 except that $\boldsymbol{w}_\beta$ now contains the downwash on all the UVLM panels.

Using the same simulation parameters, the reduction in rms of RBM through IPC was 35.8%. This is close to three times that of the baseline flap controller of 13.0% reduction and almost similar to the aggressively tuned flap controller of 32.1% reduction (See Table 3). This is not surprising as IPC involves actuating the whole blade, resulting in larger aerodynamic forces than those achievable from flaps. It should also be noted that the performance of IPC is lower than that of the combined active flap and bend-twist coupling, which delivered above 40% reduction in loads as shown in Table 4.

Typically, the full wind field contains a stochastic component related to turbulence and a deterministic component, which can originate from shear and tower shadow [Bergami and Henriksen(2012)]. The knowledge of this deterministic load can provide the necessary frequency information for feed-forward control through Cyclic Pitch (CPC). Often, CPC is tuned to address the peak in 1P load, which have a huge bearing on overall fatigue loads. This is achieved by prescribing harmonic pitching motion on the blades at the frequency of turbine rotation, with a 120° phase difference between the blades. For the wind profile considered with power law wind shear exponent of 0.2, the maximum achievable performance through CPC was 12.5% reduction in rms of RBM, with a maximum pitch rate of $1.5°/s$. The PSD of RBM on one of the rotor blades in closed-loop with IPC and CPC is shown in Figure 20, where it is evident that the reductions through IPC is across most frequencies while CPC is focused on suppressing only the 1P loads.

While pitch controls deliver better performances than flaps, the power required by the former is expected to be much higher and increases with blade size, with the pitch mechanism having to overcome the inertia of the entire blade. There will also be increased wear and tear in pitch bearings [Plumley et al.(2014)Plumley, Leithead, Jamieson,
It should be noted that in line with the controller design for active flaps, the IPC and CPC controllers here are synthesized from a single rotating blade and neglected any interference the pitch mechanisms may have with other control objectives, such as those of pitch regulation for speed controls [Bossanyi(2003)].

5 Conclusions

The aeroelastic response and gust load alleviation of a large wind turbine has been numerically investigated using models obtained from coupling composite beams with vortex-lattice-based aerodynamics written in state-space form. The

finite-element solution of the rotor blades is linearized around large geometrically-nonlinear rotating equilibrium conditions. The connection between the rotor hub and tower, including prescribed rotations are enforced through Lagrange multipliers. The aerodynamics is modeled using the unsteady vortex-lattice method, that allows the kinematics of large turbines blades to be captured with higher fidelity than blade-element momentum theory and captures spanwise aerodynamic effects of control surfaces. Through modal decomposition of the structural equations of motion and balanced truncation of the aerodynamics, the size of the resulting coupled aeroelastic model has been reduced to speed up computation time by more than two orders of magnitude. For the structural modal decomposition, higher frequency mode shapes were seen to play a crucial role in capturing the correct steady-state torsional amplitudes, despite the dynamics already being captured with smaller number of modes.

Using the NREL 5-MW wind turbine as a test case, the viability of this computational approach was demonstrated. First, it allowed an investigation on aeroelastic tailoring through bend-twist coupling (twist-towards-feather), and was shown to deliver significant reductions in blade and tower loads. Subsequently, the turbine blade model was fitted with trailing-edge flaps. Using $\mathcal{H}_\infty$ controllers with root-bending moment feedback synthesized from a single clamped rotating blade, a closed-loop root-mean-square reduction of 13% in blade loads, 16% reduction in maximum blade tip flapwise deflection and 11% root-mean-square reduction in tower fore-aft deflection were observed. In this full turbine simulation, the flap deflections were initially kept within the bounds of $\pm 10^\circ$. However, using more aggressive controllers in the presence of actuator saturation in the full turbine model, performance in terms of reduction in root-mean-square values can be doubled, even though the effect on reduction in maximum values was smaller. It was also shown that root-mean-square values were more affected by limits on $\dot{\beta}$ while maximum values were bounded by β. The possibility of 'moment flaps' was also considered and indicated the need to reduce blade torsional stiffness below 30% before control reversal was observed, highlighting that the concept of 'moment flaps' may not be effective on a conventional wind turbine blade structure. However, a relatively small reduction in torsional stiffness was seen to add damping to the low frequency flap modes and this may have a beneficial effect on fatigue life. Importantly, synergies between passive and active mechanisms were possible and they were demonstrated through the combined bend-twist coupling and active flap control. This integrated concept was capable of reducing loads in terms of root-mean-square and maximum values by almost half, with passive load alleviation targeting the lower end of the frequency load spectrum (below 3P) and flaps acting on the higher frequencies. Pitch controls was also considered and delivered slightly higher load reductions than flaps alone. However. the latter have the advantage of being lighter in weight, lower in energy consumption and with faster actuation speeds.

While the benefit of passive load alleviation is evident, the approach here had assumed that both the bending and torsional stiffnesses remained unchanged through the process of elastic coupling. This increases the overall stiffness of the elastically coupled blades, and detailed composite lay-up analysis are still needed to correctly capture the stiffness values. Moreover, for active flap control, actuator dynamics have not been included and hence the load alleviation efficiency is expected to be lower in actual implementation. Overall, the current

combination of passive load alleviation and active flap control have been shown to be an effective strategy for fatigue load reduction.

6 Acknowledgments

The work of Bing Feng Ng is funded by the Energy Innovation Programme Office, Singapore, and appreciates their support. The work of Henrik Hesse was sponsored by the UK Engineering and Physical Sciences Research Council (grant number EP/I014683/1).

References

[Barlas and van Kuik(2010)] T. K. Barlas and G. A. M. van Kuik. Review of state of the art in smart rotor control research for wind turbines. *Progress in Aerospace Sciences*, 46(1):1–27, 2010. doi: 10.1016/j.paerosci.2009.08.002.

[Barlas et al.(2012)Barlas, van der Veen, and van Kuik] T. K. Barlas, G. J. van der Veen, and G. A. M. van Kuik. Model predictive control for wind turbines with distributed active flaps: Incorporating inflow signals and actuator constraints. *Wind Energy*, 15(5):757–771, 2012. doi: 10.1002/we.503.

[Barlas et al.(2013)Barlas, van Wingerden, Hulskamp, van Kuik, and Bersee] T. K. Barlas, W. van Wingerden, A. W. Hulskamp, G. A. M. van Kuik, and H. E. N. Bersee. Smart dynamic rotor control using active flaps on a small-scale wind turbine: Aeroelastic modeling and comparison with wind tunnel measurements. *Wind Energy*, 16(8):1287–1301, 2013. doi: 10.1002/we.1560.

[Berg et al.(2009)Berg, Wilson, Resor, Barone, and Berg] D. E. Berg, D. G. Wilson, B. R. Resor, M. F. Barone, and J. C. Berg. Active aerodynamic blade load control impacts on utility-scale wind turbines. In *Proceedings of the AWEA Windpower*, Chicago, IL, USA, 2009.

[Bergami and Henriksen(2012)] L. Bergami and L. C. Henriksen. Cyclic control optimization for a smart rotor. In *Proceedings of the 8th PhD Seminar on Wind Energy in Europe 2012*, Zurich, Switzerland, 2012.

[Bergami and Poulsen(2014)] L. Bergami and N. K. Poulsen. A smart rotor configuration with linear quadratic control of adaptive trailing edge flaps for active load alleviation. *Wind Energy*, 2014. doi: 10.1002/we.1716.

[Bergami et al.(2014)Bergami, Riziotis, and Gaunaa] L. Bergami, V. A. Riziotis, and M. Gaunaa. Aerodynamic response of an airfoil section undergoing pitch motion and trailing edge flap deflection: a comparison of simulation methods. *Wind Energy*, 2014. doi: 10.1002/we.1759.

[Bossanyi(2003)] E. A. Bossanyi. Individual blade pitch control for load reduction. *Wind Energy*, 6(2):119–128, 2003. doi: 10.1002/we.76.

[Bottasso et al.(2013)Bottasso, Campagnolo, Croce, and Tibaldi] C. L. Bottasso, F. Campagnolo, A. Croce, and C. Tibaldi. Optimization-based

study of bend-twist coupled rotor blades for passive and integrated passive/active load alleviation. *Wind Energy*, 16(8):1149–1166, 2013. doi: 10.1002/we.1543.

[Bottasso et al.(2014)Bottasso, Cacciola, and Riva] C. L. Bottasso, S. Cacciola, and R. Riva. Floquet stability analysis of wind turbines using input-output models. In *Proceedings of AIAA Scitech - 32nd ASME Wind Energy Symposium*, National Harbor, MD, USA, 2014. doi: 10.2514/6.2014-0713.

[Burton(2011)] T. Burton. *Wind energy handbook*. Wiley, Chichester, UK, 2nd edition, 2011.

[Castaignet et al.(2013)Castaignet, Couchman, Poulsen, Buhl, and Wedel-Heinen] D. Castaignet, I. Couchman, N. K. Poulsen, T. Buhl, and J. J. Wedel-Heinen. Frequency-weighted model predictive control of trailing edge flaps on a wind turbine blade. *IEEE Transaction on Control Systems Technology*, 21(4), 2013. doi: 10.1109/TCST.2013.2260750.

[Castaignet et al.(2014)Castaignet, Barlas, Buhl, Poulsen, Wedel-Heinen, Olesen, Bak, and Kim] D. Castaignet, T. Barlas, T. Buhl, N. K. Poulsen, J. J. Wedel-Heinen, N. A. Olesen, C. Bak, and T Kim. Full-scale test of trailing edge flaps on a Vestas V27 wind turbine: Active load reduction and system identification. *Wind Energy*, 17(4):549–564, 2014. doi: 10.1002/we.1589.

[Chattot(2007)] J-J. Chattot. Helicoidal vortex model for wind turbine aeroelastic simulation. *Computers and Structures*, 85(11-14):1072–1079, 2007. doi: 10.1016/j.compstruc.2006.11.013.

[Chopra and Sirohi(2014)] I. Chopra and J. Sirohi. *Smart Structures Theory*. Cambridge University Press, New York, USA, 2014.

[Cook et al.(2013)Cook, Palacios, and Goulart] R. G. Cook, R. Palacios, and P. J. Goulart. Robust gust alleviation and stabilization of very flexible aircraft. *AIAA Journal*, 51(2):330–340, 2013. doi: 10.2514/1.J051697.

[Dizy et al.(2013)Dizy, Palacios, and Phino] J. Dizy, R. Palacios, and S. T. Phino. Homogenisation of slender periodic composite structures. *International Journal of Solids and Structures*, 50(9), 2013. doi: 10.1016/j.ijsolstr.2013.01.017.

[Frederick et al.(2010)Frederick, Kerrigan, and Graham] M. Frederick, E. C. Kerrigan, and J. M. R. Graham. Gust alleviation using rapidly deployed trailing-edge flaps. *Journal of Wind Engineering and Industrial Aerodynamics*, 98(12):712–723, 2010. doi: 10.1016/j.jweia.2010.06.005.

[Freebury and Musial(2000)] G. Freebury and W. Musial. Determining equivalent damage loading for full-scale wind turbine blade fatigue tests. In *Proceedings of the 19th American Society of Mechanical Engineers Wind Energy Symposium*, Reno, NV, USA, 2000.

[Géradin and Cardona(2001)] M. Géradin and A. Cardona. *Flexible multibody dynamics: A finite element approach*. John Wiley, Chichester, England; New York, USA, 2001.

[Géradin and Rixen(1997)] M. Géradin and D. Rixen. *Mechanical vibrations: Theory and application to structural dynamics*. John Wiley, Chichester, England; New York, USA, 2nd edition, 1997.

[Geyler and Caselitz(2008)] M. Geyler and P. Caselitz. Robust multivariable pitch control design for load reduction on large wind turbines. *Journal of solar energy engineering*, 130(3):031014, 2008. doi: 10.1115/1.2931510.

[Gupta and Leishman(2005)] S. Gupta and J. G. Leishman. Comparison of momentum and vortex methods for the aerodynamic analysis of wind turbines. In *Proceedings of the 43rd AIAA Aerospace Sciences Meeting and Exhibition*, Reno, NV, USA, 2005. doi: 10.2514/6.2005-594.

[Hansen et al.(2006)Hansen, Sørensen, Voutsinas, Sørensen, and Madsen] M.O.L. Hansen, J. N. Sørensen, S. G. Voutsinas, N. Sørensen, and H. A. Madsen. State of the art in wind turbine aerodynamics and aeroelasticity. *Progress in Aerospace Sciences*, 42(4):285–330, 2006. doi: 10.1016/j.paerosci.2006.10.002.

[Hauptmann et al.(2013)Hauptmann, Bülk, Erbslöh, Boorsma, Grasso, Kühn, and Cheng] S. Hauptmann, M. Bülk, S. Erbslöh, K. Boorsma, F. Grasso, M. Kühn, and P. W. Cheng. Impact of the lifting-line free vortex wake method on the simulated loads of multi-MW wind turbines. In *The Science of Making Torque from Wind*, Oldenburg, Germany, 2013.

[Hayman()] G. Hayman. NWTC Design Codes (MLife). Last modified 22-October-2012; Accessed 5-February-2014. http://wind.nrel.gov/designcodes/postprocessors/MLife/.

[Hendriks and Bulder(1995)] H. B. Hendriks and B. H. Bulder. Fatigue equivalent load cycle method - a general method to compare the fatigue loading of different load spectrums. Technical report, ECN-C-95-074, 1995.

[Henriksen et al.(2013)Henriksen, Bergami, and Andersen] L. C. Henriksen, L. Bergami, and P.B. Andersen. A model based control methodology combining blade pitch and adaptive trailing edge flaps in a common framework. In *Proceedings of the EWEC*, Vienna, Austria, 2013.

[Hesse and Palacios(2012)] H. Hesse and R. Palacios. Consistent structural linearisation in flexible-body dynamics with large rigid-body motion. *Computers and Structures*, 110-111(0):1–14, 2012. doi: 10.1016/j.compstruc.2012.05.011.

[Hesse and Palacios(2014)] H. Hesse and R. Palacios. Reduced-order aeroelastic models for the dynamics of maneuvering flexible aircraft. *AIAA Journal*, 52(8), 2014. doi: 10.2514/1.J052684.

[Hodges and Pierce(2002)] D. H. Hodges and G. A. Pierce. *Introduction to structural dynamics and aeroelasticity*. Cambridge aerospace series. Cambridge University Press, Cambridge, England; New York, USA, 2002.

[IEC 61400-1(2006)] IEC 61400-1. Wind turbines-part 1: Design requirements. Technical report, International Electrotechnical Commission, 2006.

[Jonkman and Kilcher()] B. J. Jonkman and L. Kilcher. NWTC Computer-Aided Engineering Tools (TurbSim). Last modified 30-May-2013; accessed 5-February-2014. http://wind.nrel.gov/designcodes/preprocessors/turbsim/.

[Jonkman et al.(2009)Jonkman, Butterfield, Musial, and Scott] J. Jonkman, S. Butterfield, W. Musial, and G. Scott. Definition of a 5-MW wind turbine for offshore system development. Technical report, NREL/TP-500-38060, 2009.

[Katz and Plotkin(2001)] J. Katz and A. Plotkin. *Low speed aerodynamics*. Cambridge aerospace series. Cambridge University Press, Cambridge, UK; New York, USA, 2nd edition, 2001.

[Larsen et al.(2005)Larsen, Madsen, and Thomsen] T. J. Larsen, H.A. Madsen, and K. Thomsen. Active load reduction using individual pitch, based on local blade flow measurements. *Wind Energy*, 8(1):67–80, 2005. doi: 10.1002/we.141.

[Leishman(2002)] J. G. Leishman. Challenges in modeling the unsteady aerodynamics of wind turbines. In *Proceedings of the 21st ASME Wind Energy Symposium*, Reno, NV, USA, 2002.

[Leithead et al.(2009)Leithead, Neilson, Dominguez, and Dutka] W. E. Leithead, V. Neilson, S. Dominguez, and A. Dutka. A novel approach to structural load control using intelligent actuators. In *Proceedings of the 17th Mediterranean Conference on Control and Automation*, Makedonia Palace, Thessaloniki, Greece, 2009. doi: 10.1109/MED.2009.5164719.

[Lobitz and Veers(2003)] D. W. Lobitz and P. S. Veers. Load mitigation with bending/twist-coupled blades on rotors using modern control strategies. *Wind Energy*, 6(2):105–117, 2003. doi: 10.1002/we.74.

[Lu et al.(2014)Lu, Bowyer, and Jones] Q. Lu, R. Bowyer, and B. L. Jones. Analysis and design of Colemen transform-based individual pitch controllers for wind turbine load reduction. *Wind Energy*, 2014. doi: 10.1002/we.1769.

[Murua et al.(2012a)Murua, Palacios, and Graham] J. Murua, R. Palacios, and J. M. R. Graham. Applications of the unsteady vortex-lattice method in aircraft aeroelasticity and flight dynamics. *Progress in Aerospace Sciences*, 55:46–72, 2012a. doi: 10.1016/j.paerosci.2012.06.001.

[Murua et al.(2012b)Murua, Palacios, and Graham] J. Murua, R. Palacios, and J. M. R. Graham. Assessment of wake-tail interference effects on the dynamics of flexible aircraft. *AIAA Journal*, 50(7):1575–1585, 2012b. doi: 10.2514/1.J051543.

[Ng et al.(2013)Ng, Hesse, Palacios, Graham, and Kerrigan] B. F. Ng, H. Hesse, R. Palacios, J. M. R. Graham, and E. C. Kerrigan. Aeroservoelastic modeling and load alleviation of very large wind turbine blades. In *AWEA Windpower*, Chicago, IL, USA, 2013.

[Ng et al.(2014)Ng, Hesse, Palacios, Graham, and Kerrigan] B. F. Ng, H. Hesse, R. Palacios, J. M. R. Graham, and E. C. Kerrigan. Aeroservoelastic state-space vortex lattice modeling and load alleviation of wind turbine blades. *Wind Energy*, 2014. doi: 10.1002/we.1752.

[Ozdemir et al.(2011)Ozdemir, Seiler, and Balas] A. A. Ozdemir, P. J. Seiler, and G. J. Balas. Performance of disturbance augmented control design in turbulent wind conditions. *Mechatronics*, 21(4):634–644, 2011. doi: 10.1016/j.mechatronics.2011.01.008.

[Palacios and Cesnik(2005)] R. Palacios and C. Cesnik. Cross-sectional analysis of non-homogeneous anisotropic active slender structures. *AIAA Journal*, 43(12):2624–2638, 2005. doi: 10.2514/1.12451.

[Palacios et al.(2010)Palacios, Murua, and Cook] R. Palacios, J. Murua, and R. Cook. Structural and aerodynamic models in the nonlinear flight dynamics of very flexible aircraft. *AIAA Journal*, 48(11):2559–2648, 2010. doi: 10.2514/1.J050513.

[Plumley et al.(2014)Plumley, Leithead, Jamieson, Bossanyi, and Graham] C. Plumley, W. Leithead, P. Jamieson, E. Bossanyi, and J. M. R. Graham. Comparison of individual pitch and smart rotor control strategies for load reduction. *Journal of Physics Conference Series: The Science of Making Torque from Wind*, 524:012054, 2014. doi: 10.1088/1742-6596/524/1/012054.

[Shirk et al.(1986)Shirk, Hertz, and Weisshaar] M. Shirk, T. Hertz, and T. Weisshaar. Aeroelastic tailoring: Theory, practice and promise. *Journal of Aircraft*, 23(1), January 1986.

[Simo and Vu-Quoc(1988)] J. C. Simo and L. Vu-Quoc. On the dynamics in space of rods undergoing large motions - a geometrically exact approach. *Computer Methods in Applied Mechanics and Engineering*, 66(2):125–161, 1988. doi: 10.1016/0045-7825(88)90073-4.

[Simoes and Graham(1992)] F. J. Simoes and J. M. R. Graham. Application of a free vortex wake model to a horizontal axis wind turbine. *Wind Engineering and Industrial Aerodynamics*, 39(1-3):129–138, 1992. doi: 10.1016/0167-6105(92)90539-M.

[Skjoldan(2011)] P. F. Skjoldan. *Aeroelastic modal dynamics of wind turbines including anisotropic effects*. PhD thesis, Technical University of Denmark, 2011.

[Skogestad and Postlethwaite(2005)] S. Skogestad and I. Postlethwaite. *Multivariable feedback control: Analysis and design*. John Wiley, Chichester, England; Hoboken, NJ, USA, 2nd edition, 2005.

[Vesel Jr and McNamara(2014)] Richard. W. Vesel Jr and Jack. J. McNamara. Performance enhancement and load reduction of a 5 MW wind turbine blade. *Renewable Energy*, 66:391–401, 2014. doi: 10.1016/j.renene.2013.12.019.

[Voutsinas(2006)] Spyros G. Voutsinas. Vortex methods in aeronautics: How to make things work. *International Journal of Computational Fluid Dynamics*, 20(1):3–18, 2006. doi: 10.1080/10618560600566059.

[Welch(1967)] P. D. Welch. The use of fast fourier transform for the estimation of power spectra: A method based on time averaging over short, modified periodograms. *IEEE Trans. Audio Electroacoustic*, AU-15(2), 1967. doi: 10.1109/TAU.1967.1161901.

[Wilson et al.(2009)Wilson, Berg, Resor, Barone, and Berg] D. G. Wilson, D. E. Berg, B. R. Resor, M. F. Barone, and J. C. Berg. Combined individual pitch control and active aerodynamic load controller investigation for the 5MW UpWind turbine. In *Proceedings of the AWEA Windpower*, Chicago, IL, USA, 2009.

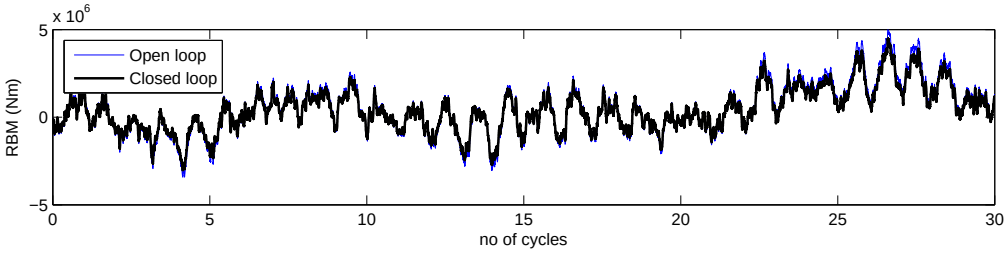

(a) Blade flapwise RBM.

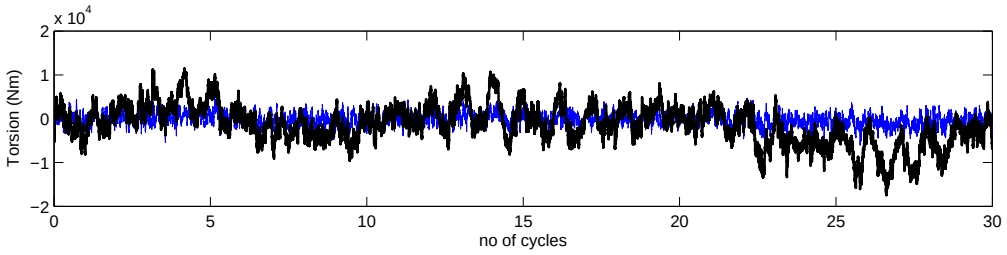

(b) Blade root torsion.

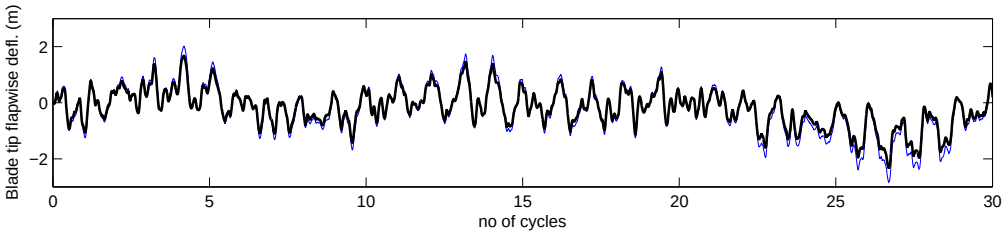

(c) Blade tip flapwise deflection.

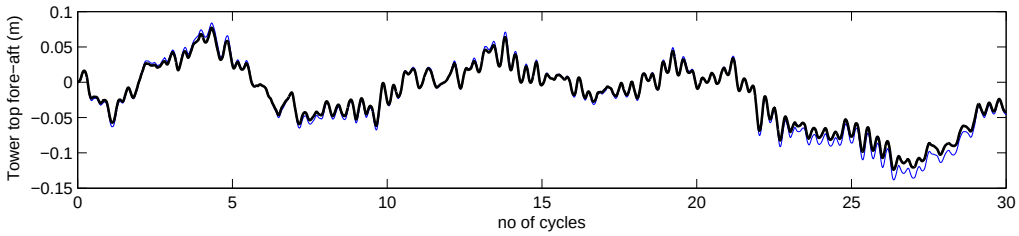

(d) Tower top fore-aft deflection.

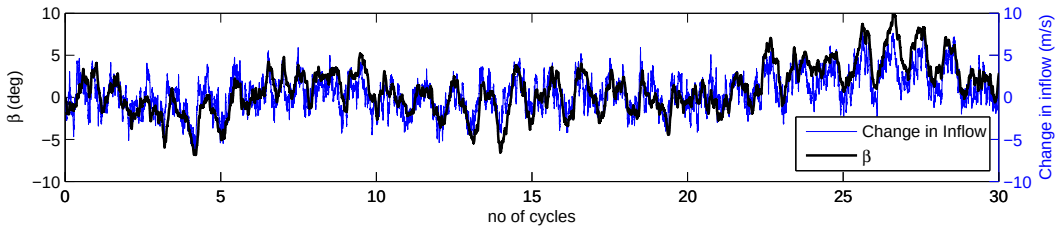

(e) Flap deflection angle and change in inflow at the blade tip during rotation.

Figure 13: Section of measurement time-series for the full wind turbine configuration without elastic coupling. Closed-loop is when trailing-edge flaps are activated.

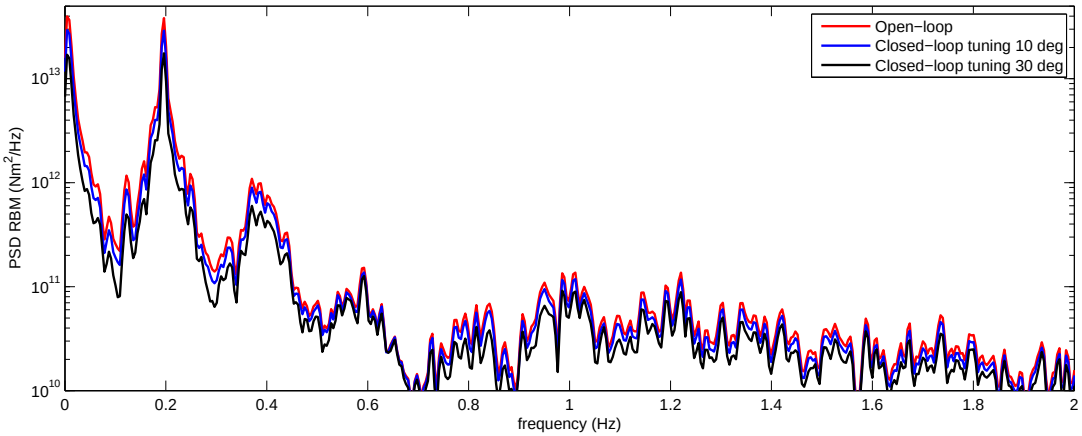

Figure 14: PSD of flapwise RBM on one of the rotor blades in open/closed-loop comparing controllers tuned to 10° and 30°. Closed-loop is when trailing-edge flaps are activated and the blades are without elastic coupling.

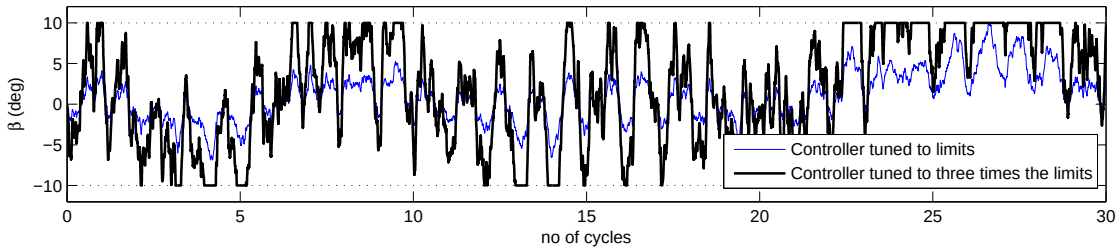

Figure 15: Closed-loop flap deflection angle using different controllers with tuning on maximum $|\beta|$ to the limit of 10° and 30°.

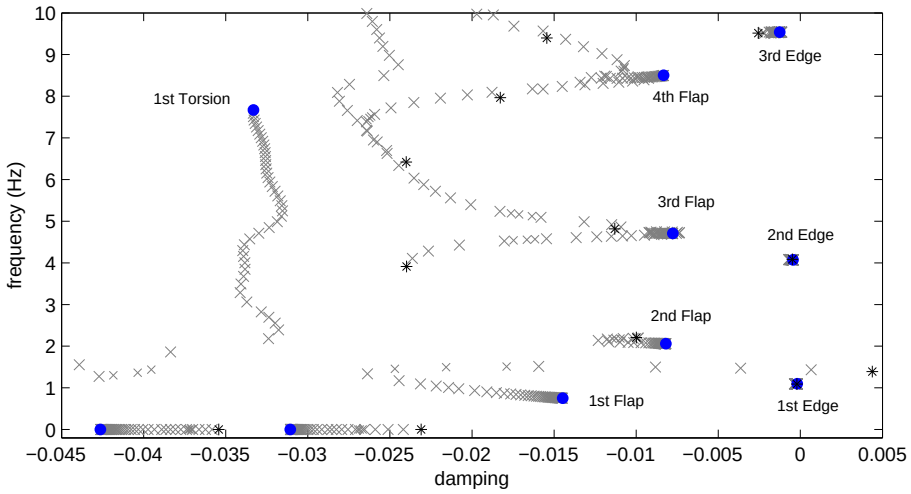

Figure 16: Root locus on a single NREL blade as torsional stiffness is reduced from original value (blue circle) to 14% stiffness (black star) in intervals of 2%.

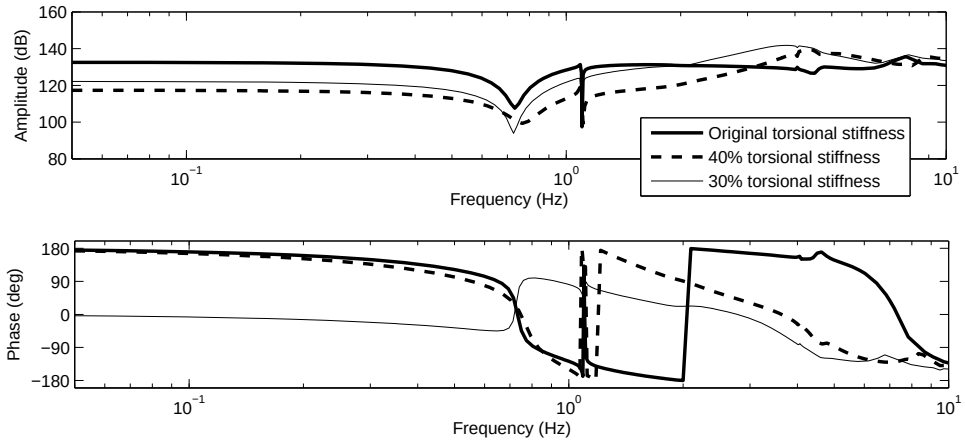

Figure 17: Bode plot from flap input to blade flapwise RBM on the NREL blade as torsional stiffness is reduced. A 180° phase change is observed when torsional stiffness is reduced to 30%.

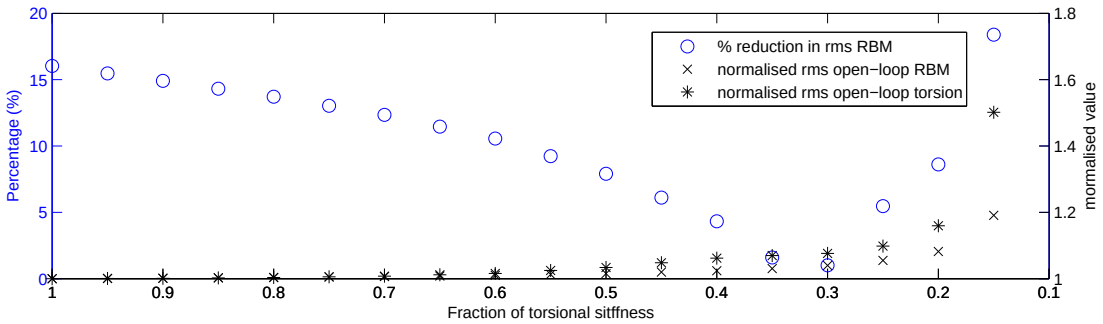

Figure 18: Percentage reduction in RBM and normalized open-loop rms values as torsional stiffness is reduced on a single rotating blade.

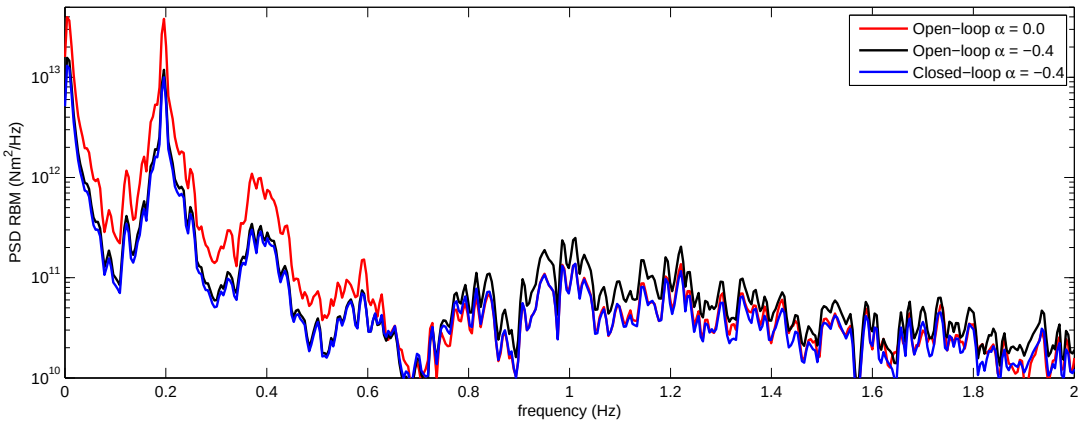

Figure 19: PSD of RBM on one of the rotor blades in open/closed-loop with and without elastic coupling. Open-loop α = -0.4 is with bend-twist coupling only. Closed-loop α = -0.4 is with bend-twist coupling and trailing-edge flaps.

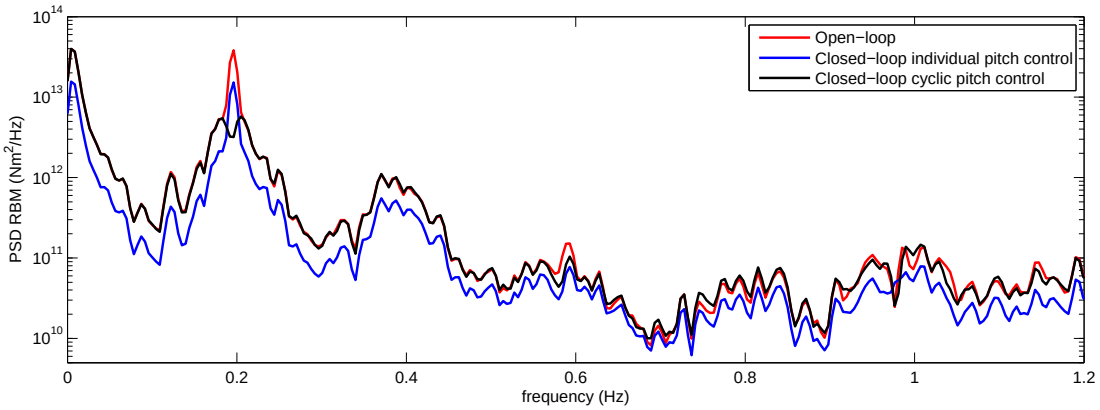

Figure 20: PSD of RBM on one of the rotor blades in open/closed-loop with individual pitch control and cyclic pitch control.